



Development of secondary vortex structures in rotor wakes

Clemens Schwarz¹ · Andrew Bodling² · C. Christian Wolf¹ · Robert Brinkema¹ · Mark Potsdam³ · Anthony D. Gardner¹

Received: 29 June 2021 / Revised: 1 October 2021 / Accepted: 24 October 2021 / Published online: 6 December 2021
© The Author(s) 2021

Abstract

The blade tip vortex system is a crucial feature in the wake of helicopter rotors, and its correct prediction represents a major challenge in the numerical simulation of rotor flows. A common phenomenon in modern high-fidelity CFD simulations is the breakdown of the primary vortex system in hover due to secondary vortex braids. Since they are strongly influenced by the numerical settings, the degree to which these secondary vortex structures actually physically occur is still discussed and needs experimental validation. In the current work, the development of secondary vortex structures in the wake of a two-bladed rotor in hover conditions was investigated by combining stereoscopic particle image velocimetry measurements in different measurement planes and high-fidelity simulations. Secondary vortex structures were detected and quantified at different axial locations in the wake by applying an identical scheme to the measured and simulated velocity data. In agreement, it was found that the number of secondary vortices is maximum at a distance of $0.8 R$ below the rotor. The more intense secondary vortex structures were quantitatively well captured in the simulation, whereas in the experiment a larger number of weaker vortices were detected. No distinct preferential direction of rotation was found for the secondary vortices, but they tended to develop in vortex pairs with alternating sense of rotation. A clustered occurrence of secondary vortices was observed close to the primary tip vortices, where the rolled-up blade shear layer breaks down into coherent vortex structures.

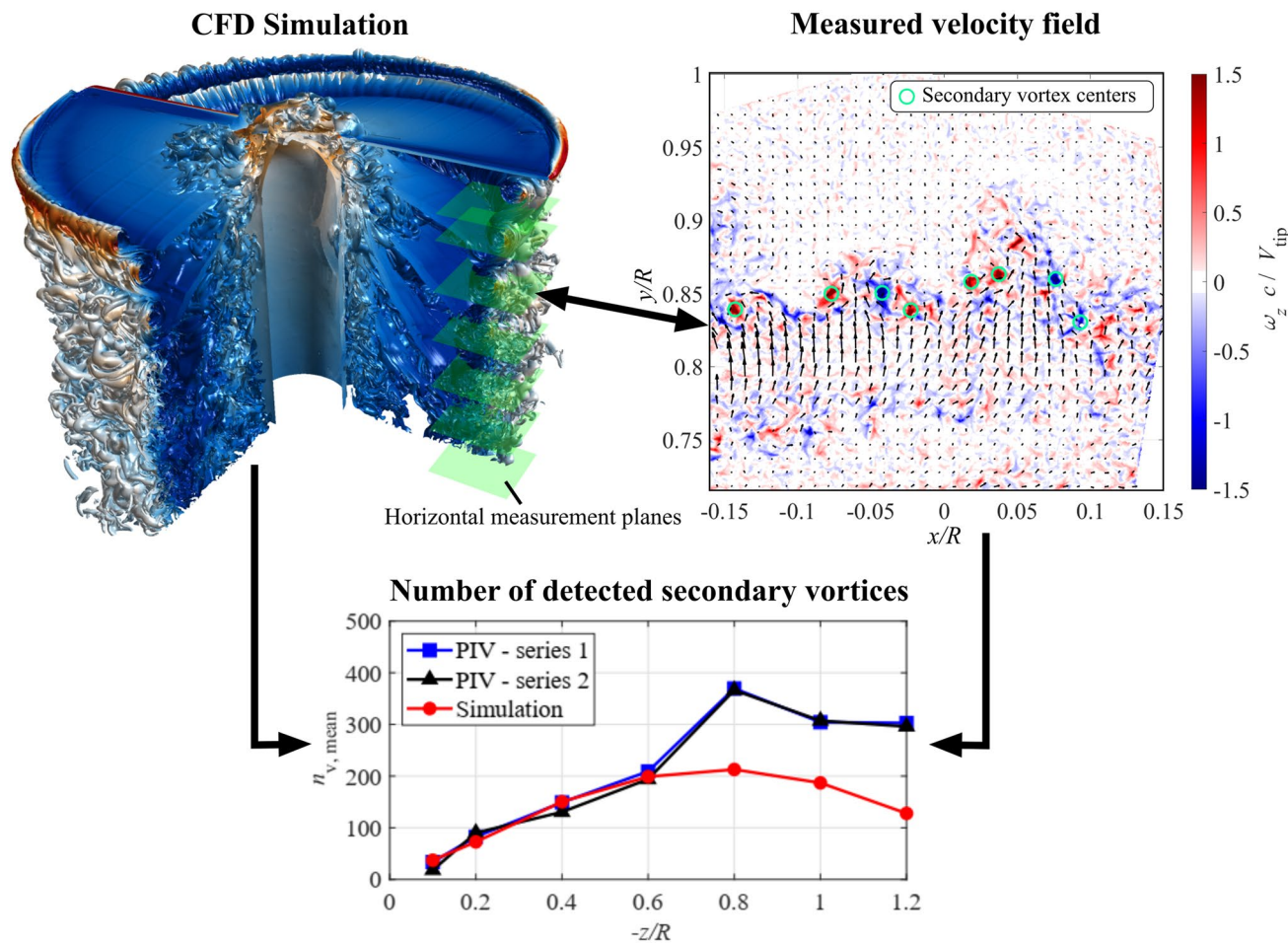
✉ Clemens Schwarz
clemens.schwarz@dlr.de

¹ German Aerospace Center (DLR), Institute of Aerodynamics and Flow Technology, Göttingen, Germany

² Science and Technology Corporation, Moffett Field, CA, USA

³ U.S. Army Combat Capabilities Development Command, Aviation and Missile Center, Moffett Field, CA, USA

Graphical abstract



List of symbols

c	Blade chord length, $c = 0.061 \text{ m}$	V_h	Hover-induced velocity, $V_h = V_{\text{tip}} \sqrt{\frac{C_T}{2}} \text{ (m/s)}$
c_{tip}	Chord length at the blade tip, $c_{\text{tip}} = 0.0419 \text{ m}$	V_{tip}	Rotor tip speed, $V_{\text{tip}} = \Omega R = 101.76 \text{ m/s}$
C_T	Thrust coefficient, $C_T = T / (\rho \pi \Omega^2 R^4)$	V_{xy}	Absolute velocity
k	Normalized turbulent kinetic energy	V_{yz}	Velocity in the y, z -plane
k_x, k_y, k_z	Cartesian components of k , Eq. 2	V_Θ	Swirl velocity around vortex center (m/s)
k_{yz}	Component of k in the y, z -plane, Eq. 1	$V_{\Theta,\text{max}}$	Maximum swirl velocity (m/s)
$n_{v,\text{mean}}$	Mean vortex number per sample and 360°	x, y, z	Coordinates in the reference frame (m)
N_b	Number of blades, $N_b = 2$	Γ	Circulation (m^2/s)
Q	Q -criterion, Eq. 3 ($1/\text{s}^2$)	Γ_v	Vortex circulation at large distances (m^2/s)
Q_s	Signed Q -criterion, $Q_s = Q \cdot \frac{\omega_z}{ \omega_z } (1/\text{s}^2)$	λ	Signed swirling strength ($1/\text{s}$)
r	Radial coordinate (m)	λ_2	Eigenvalues of the velocity gradient tensor ($1/\text{s}^2$)
r_c	Vortex core radius (m)	ν	Kinematic viscosity (m^2/s)
R	Rotor radius, $R = 0.775 \text{ m}$	ρ	Air density (kg/m^3)
Re_v	Vortex Reynolds number, $\text{Re}_v = \Gamma_v / \nu$	σ	Rotor solidity, $\sigma = N_b c / \pi R = 0.05$
t	Time (s)	ψ	Wake age ($^\circ$)
T	Rotor thrust (N)	ω	Vorticity ($1/\text{s}$)
u, v, w	Velocities in the x -, y -, z -directions (m/s)	ω_z	Vorticity normal to x, y -plane ($1/\text{s}$)
		Ω	Angular velocity of the rotor, $\Omega = 131.3 \text{ rad/s}$

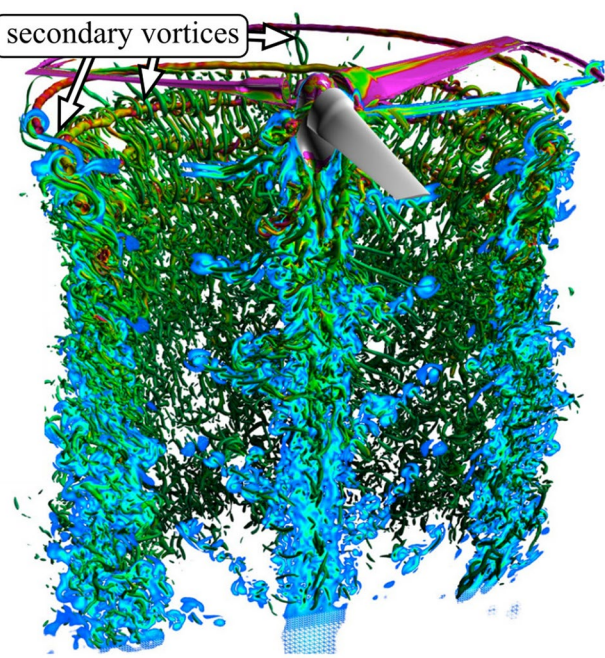


Fig. 1 Three-bladed TRAM OVERFLOW simulation by Chaderjian and Buning (2011)

1 Introduction

The wake of a helicopter rotor is a three-dimensional unsteady flow, which is challenging to understand even with modern experimental and numerical methods. The flow is characterized by a system of blade tip vortices and blade shear layers which convect downstream in the rotor downwash. To model the rotor flow in numerical simulations and accurately predict the aerodynamic parameters of the rotor, the structure and strength of the blade tip vortex system must be correctly represented. Particularly, the breakdown of the wake and its effect on the rotor performance as well as on complex interactional aerodynamics is still a subject that needs further investigation. An issue raised by recent high-fidelity CFD simulations is the role of secondary vortex structures in the collapse of the blade tip vortex system. Such smaller secondary vortex braids spanning between the blade tip vortices were first observed by Chaderjian and Buning (2011). An example OVERFLOW simulation of the 3-bladed TRAM rotor exhibiting secondary worms is depicted in Fig. 1. These structures became a frequently observed phenomenon in simulations as high-order methods and finer grids became the state of the art (Hariharan et al. 2014; Potsdam and Jayaraman 2014; Jain 2018; Öhrle et al. 2018; Abras et al. 2019). The appearance of these structures triggered a discussion whether they are an actual physical phenomenon or a purely numerical artifact connected to an insufficient

convergence in the simulations. (See, for example, Egolf et al. (2017) and Hariharan et al. (2020).)

Chaderjian argues that the secondary vortices originate from the vorticity contained in the blade shear layer perpendicular to the vortex core (Chaderjian 2012). The axial stretching that results from a part of the shear layer being entrained into the preceding blade tip vortex subsequently augments the worms' rotation due to conservation of momentum. The emergence of the secondary vortex braids/worms bridging between the helical tip vortex strands results in a transfer of energy from a large scale to small scale, which resembles the instability mechanisms of mixing layers (Bernal and Roshko 1986; Comte et al. 1998).

Despite the physical plausibility of secondary vortices as a sign of instability braids spanning between closely convecting blade tip vortex filaments, their strength and the extent to which these vortices contribute to the breakdown of the primary vortex system are still not clear (Hariharan et al. 2020). A study by Abras et al. (2019) demonstrated that the occurrence and structure of the secondary vortices in CFD rotor studies are largely dependent on the simulation time and on the numerical setup including mesh resolution or turbulence model. In a grid study, both rotating and stationary torus grids and Cartesian grids were used with different grid densities to investigate how these grid topologies influence the physical flow features and presence of complete wake breakdown. The authors term this event “vortex soup” and discuss countermeasures applicable to the CFD setup. Recent numerical investigations also addressed the effect of time marching on secondary vortex braids and wake breakdown (Lee and Baeder 2021) and investigated volume rendering techniques for a better understanding of the phenomenon (Abras and Hariharan 2021). Additionally, proper orthogonal decomposition was used to analyze the wake breakdown (Mobley et al. 2021).

While the parameters and development of the primary blade tip vortices were measured and characterized in a variety of previous studies (for example Heineck et al. 2000; Ramasamy et al. 2009b; Mula et al. 2013), experimental evidence for the existence of secondary vortices was very sparse in the past. Although indications of secondary vortices can be found in smoke visualizations by Gray (1992), explicit experimental proof for their existence was only provided in a recent volumetric flow measurement by Wolf et al. (2019b) in the wake of a two-bladed and highly loaded model helicopter in ground effect. The tests were conducted using the “Shake-The-Box”-method (Schanz et al. 2016), which is a time-resolved and volumetric variant of particle image velocimetry (PIV, see Raffel et al. (2017)). A sample result from these measurements is depicted in Fig. 2a. The secondary worms that span between the gray blade tip vortices are visualized using Q -isosurfaces that are colored red or blue depending on the vortices sense of rotation. Vortices

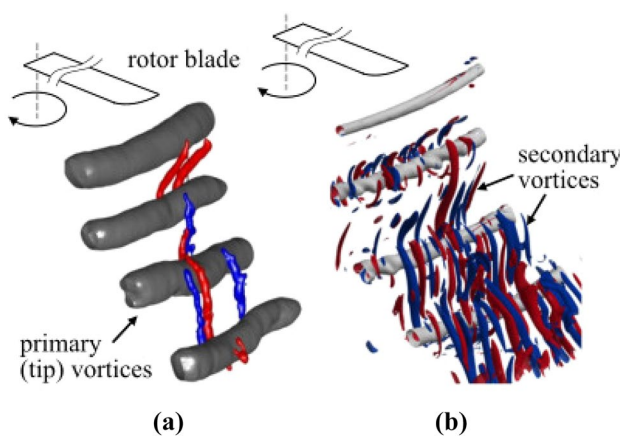


Fig. 2 Secondary vortex structures as seen in experiments (a) and CFD simulations (b) (Wolf et al. 2019b; Bodling and Potsdam 2020)

with different sense of rotation were observed that were created shortly downstream of the rotor blades starting at wake ages of approximately 75° .

Later, a detailed Helios CFD study of this test case was conducted by Bodling and Potsdam (2020); see Fig. 2b. They focused on how temporal convergence affects the development of the secondary vortices, but the effect of off-body grid structure, rotation, and resolution was also studied. The main conclusion drawn from this study is that when the sub-iteration convergence or grid resolution is not high enough, the vortex sheet and primary vortex are broken down. Since the secondary vortices are developed by the interaction of the vortex sheet with the primary vortex structure, this results in fewer secondary vortices. Using a case with a relatively high sub-iteration convergence and grid resolution, the measurements and predictions showed good qualitative agreement, which included several similarities such as a mix of positive and negative secondary vortices, the width of the vortices, and the evolution of the vortices over time. However, despite the good qualitative agreement between the experimental data and the simulations, the degree to which the simulations were predicting the correct number of secondary vortices was still in question due to the lack of quantitative comparisons made. The lack of quantitative data was mainly due to the experimental restrictions imposed by the novel volumetric measurements. The achievable tracer particle density using helium-filled soap bubbles and thus the spatial resolution of the measurements was limited, possibly hampering the detection of small-scale vortex structures. Direct comparisons to the data were also complicated by uncertainties related to the experimental setup. For example, for a given rotor wake age, the measured secondary vortices would greatly vary depending on the rotor cycle. The pronounced cycle-to-cycle aperiodicity of the wake was triggered by the test enclosure, the

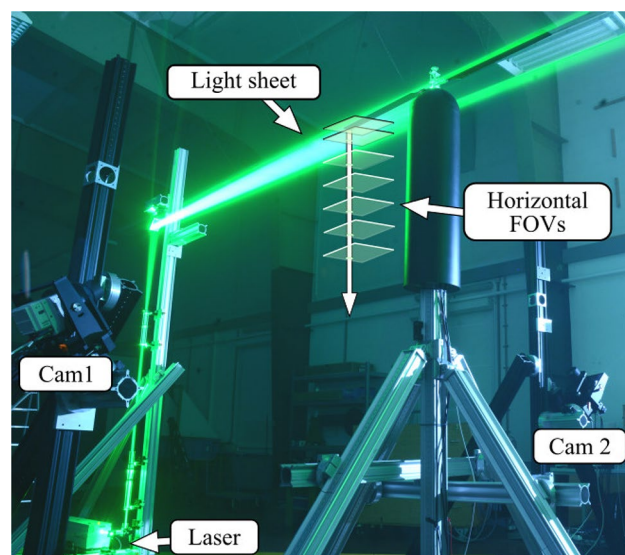


Fig. 3 Setup for PIV measurements with indicated horizontal fields of view (FOV)

asymmetric helicopter fuselage and tail rotor, etc. Therefore, a joint experimental–numerical effort with an improved setup was launched. To reduce the cycle-to-cycle variations, the same model rotor was incorporated into a new rotor test bed enabling out-of-ground-effect operation with a symmetric support structure. In order to expand the previous studies and allow for a more quantitative investigation of the secondary vortices, a high-speed stereoscopic PIV system that provides a higher spatial resolution compared to the previous “Shake-The-Box” measurements is utilized.

2 Experimental setup

2.1 Test rotor

The two-bladed test rotor had a rotor radius of $R = 0.775$ m and was operated in a laser laboratory at the German Aerospace Center (DLR) in Göttingen, Germany. The test domain is shown in Fig. 3, and the room had a dimension of about $10\text{ m} \times 12\text{ m} \times 7\text{ m}$. The rotor was mounted on a rigid support structure with a height of $4 R$ above the ground to avoid ground effect. It was equipped with two untwisted and untailed “SpinBlades Black Belt 685” rotor blades with a chord length of $c = 0.061$ m. They have a parabolic tip and a symmetrical airfoil with a thickness-to-chord ratio of 14.8%. The rotational frequency of the rotor was set to $\Omega = 131.3$ rad/s or 20.9 Hz. For the investigated test case, the rotor produced a thrust of $T = 112.8$ N, which was measured with a piezoelectric balance. This corresponds to approximately 80% of the rotor’s maximum thrust and was chosen to achieve

similar loading conditions as in the investigation by Wolf et al. (2019b) (test case 1). This results in a thrust coefficient of $C_T = T/\rho\pi\Omega^2R^4 = 0.0048$ with the air density $\rho = 1.20 \text{ kg/m}^3$, and in a blade loading of $C_T/\sigma = 0.096$. The induced velocity in hover equates to $V_h = 4.98 \text{ m/s}$. An encoder enabled a phase-locked triggering of the measurements.

2.2 Particle image velocimetry

The flow field below the rotor was studied using time-resolved stereoscopic particle image velocimetry (PIV) with an acquisition frequency of 945 double images per second or 45 images per rotor revolution. A high-speed laser with an energy output of 26 mJ/pulse and a time delay of $\Delta t = 50 \mu\text{s}$ between two pulses was used. The laser beam was expanded into a light sheet which was vertically traversed over the course of the experiment to illuminate the flow at different heights below the rotor plane. A total of 7 horizontal measurement domains ranging from $z = -0.1 R$ to $z = -1.2 R$ below the rotor plane were investigated successively. The purpose of the setup was to resolve secondary vortex structures in different stages of their development. The setup with the indicated horizontal fields of view (FOV) is depicted in Figs. 3 and 4. The FOVs had a size of about $0.3 R \times 0.3 R$ and covered about 16° of the rotor azimuth. In addition, two vertically oriented measurement planes which were stacked on top of each other were used to capture a large portion of the wake including the blade tip vortices. They both had a size of about $0.43 R \times 0.55 R$ each and are indicated as orange areas in Fig. 4. The origin of the coordinate system

that is used throughout this study is located at the rotor hub position in the rotor plane. It has to be noted that the blade tip is located in the x , y -plane only in unloaded conditions. For the rotating rotor with loaded blades, the blade tip position is about $0.026 R$ higher due to a slight coning angle.

The entire test facility was densely seeded with droplets of di-ethyl-hexyl-sebacate (DEHS) of 1.2 to $2.3 \mu\text{m}$ particle size. Both PIV cameras (Phantom VEO640L, see Fig. 3) were operated with a reduced resolution of 2176×1452 pixels and equipped with lenses with a focal length of 180 mm for the horizontal FOVs and 85 mm for the vertically oriented overview measurement planes. The resulting spatial resolution was 8.7 pixels per mm for the horizontal FOVs and 5.2 pixels per mm for the vertical FOVs.

The particle images were evaluated with Davis 8.4 (by LaVision) using multi-grid cross-correlation with a final, round interrogation window size of 16 pixels and an interrogation window overlap of 75 %. This resulted in a vector spacing of 0.46 mm ($\approx 1.1\% c_{\text{tip}}$) for the horizontal FOVs and 0.77 mm ($\approx 1.8\% c_{\text{tip}}$) for the vertical FOVs. Due to the stereoscopic camera system and a common calibration, the three-component velocity vector could be reconstructed in the measurement planes.

The PIV system was operated in two different modes for each measurement plane. First, a time-resolved series of 1000 images was recorded with the PIV system recording at a constant rate of 945 Hz, not synchronized to the rotor frequency. In the second mode, 100 batches of 40 images with a recording rate of equally 945 Hz were recorded with the first image in each batch being triggered by a 1/rev signal that was provided by the rotor encoder. This allows for an

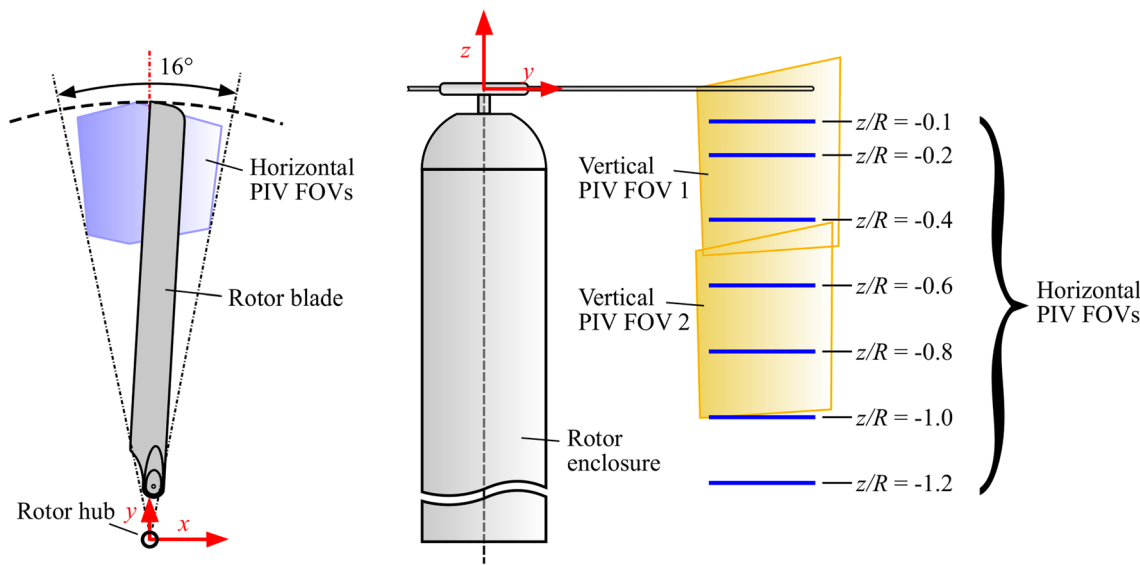


Fig. 4 Sketch of rotor setup and PIV fields of view (FOV)

assignment of the rotor azimuth to each PIV recording and for the calculation of phase-averaged velocity data ranging from an azimuthal position of 0° to 311° .

2.3 Hot-wire anemometry

Hot-wire measurements were taken complementary to the PIV investigation to allow for the determination of turbulence parameters. The hot-wire probe was a single sensor probe by TSI, type “1210-T1.5,” and was operated with a “DISA 55M” anemometer unit. The probe was operated using the constant temperature anemometry (CTA) measurement principle in which the probe was heated up to about 250°C higher temperature than the investigated fluid. With the use of a fast controlling unit, the hot wire’s resistance and thus the temperature is kept constant. The heat transfer due to convection is in turn represented by the measured voltage and is used to determine the air speed. With the low inertia of this system, high frequencies can be measured. The data were recorded at a sampling rate of 200 kHz. The response time of the hot-wire probe was around $8\ \mu\text{s}$, which leads to a theoretical bandwidth of 100 kHz. The probe was oriented parallel to the x -axis and thus measured the absolute value of the instantaneous velocity component in the y , z -plane. Measurements were taken at 7 radial positions in the wake ranging from $y/R = 0.7$ to $y/R = 1.0$ and at 34 axial locations. In the axial direction, the wake was spatially sampled in steps of 25 mm, resulting in a normalized range of $z/R = -0.0645$ to $z/R = -1.129$.

3 Numerical setup

3.1 Numerical methodology

For the simulations, Helios version 11.0 (Wissink et al. 2021) was used. Helios is the rotary wing product of the US Army and HPCMP CREATETM-AV (Air Vehicles) program sponsored by the DoD High Performance Computing Modernization Office. Helios employs an innovative multi-mesh, multi-solver paradigm for computational fluid dynamics (CFD) that uses unstructured and/or structured meshes in the “near-body” surrounding the solid surfaces to capture the wall-bounded viscous effects. Several near-body solvers are available in the latest Helios release, including unstructured mesh NSU3D, FUN3D, and kCFD; curvilinear structured mesh OVERFLOW; and strand mesh mStrand. Cartesian grids are used in the “off-body” to resolve the wake through a combination of higher-order algorithms and adaptive mesh refinement (AMR). The Cartesian meshes are managed by a block-structured mesh system which has the ability to accommodate the geometry and solution features. An overset procedure (PUNDIT) (Sitaraman et al. 2010)

facilitates the data exchange and also enables the relative motion between moving meshes. A lightweight Python-based software integration framework orchestrates the simulation and data exchange between modules. The main Helios flow solver modules used in this study are described in the following sections.

3.2 Flow solvers

3.2.1 FUN3D

The near-body solver FUN3D 13.6 (Biedron et al. 2019), an unstructured grid flow solver that has been continuously developed and supported by NASA Langley, is a node-centered, finite-volume unsteady Reynolds-averaged Navier–Stokes (URANS) solver. It is spatially second-order accurate using a Roe upwind scheme. Time-accurate computations utilize a second-order optimized backward Euler time stepping scheme along with dual-time stepping sub-iterations. The Spalart–Allmaras (SA) one-equation model with detached eddy simulation (DES) is used. FUN3D models the cylinder hub. The mixed element unstructured fuselage mesh has 1.9 M nodes. Ten sub-iterations are used, which gives a sub-iteration residual drop of at least two orders of magnitude.

3.2.2 Overflow

The near-body solver OVERFLOW 2.3b (Buning and Nichols 2021), a structured, curvilinear grid flow solver that has been continuously developed and supported by NASA Langley, is a node-centered, finite-difference URANS solver. It is a nominally spatially fifth-order accurate central difference scheme with scalar dissipation. Time-accurate computations utilize a second-order optimized backward Euler time stepping scheme along with dual-time stepping sub-iterations. The SA-DDES turbulence model with Dacles–Mariani rotation correction is used (Shur et al. 2000). OVERFLOW is used to model the rotor blades with overlapping main blade, root cap, and tip cap meshes. Each rotor blade has 10.2 M points, with 7.6 M in the main blade ($311 \times 241 \times 101$ - chordwise \times spanwise \times normal). The spacing at the outer boundary is $0.0018\ \text{m}$ ($\approx 4.3\% c_{\text{tip}}$) and extends out 1.1 chords. Fifty sub-iterations are used, which gives an average global sub-iteration residual drop of 1.65 orders of magnitude.

3.2.3 SAMCart

The Cartesian solver SAMCart is used for the off-body mesh system (Wissink et al. 2010; Pulliam 1984). SAMCart solves the Euler or Navier–Stokes equations using a fifth-order accurate central difference spatial discretization scheme for

the inviscid terms and fourth-order for the viscous terms. The solver uses an implicit second-order BDF2 LU-SGS time integration scheme. AMR can be used to accurately, efficiently, and automatically capture the features in unsteady flow based on suitable adaption criteria. User-defined rectangular regions of a particular grid resolution can also serve as input. This fixed refinement capability is used in the current effort in order to fully and uniformly capture the blade wake sheets and tip vortices. The SA-DES turbulence model with Dacles–Mariam rotation correction is used. Based off of the studies from Bodling and Potsdam (2020), having a sub-iteration residual drop of more than 1.2 orders of magnitude in the off-body solver does not seem to significantly effect the wake structure. Therefore, 10 sub-iterations are used, which gives an average sub-iteration residual drop of 1.2 orders of magnitude.

3.3 Geometry modeling, meshing, and boundary conditions

The boundary conditions at the cylinder hub and rotor blades are viscous adiabatic solid walls (i.e., no slip wall with density/pressure extrapolation). Free stream conditions are used at the farfield boundaries with an inviscid ground plane $4R$ below the rotor. The farfield boundaries are $15R$ away from the blades in each direction to avoid any boundary effects on the nearfield solution. The experiment includes a small amount of blade bending and coning, which the calculations do not account for. Since the cylinder hub should be sufficient to capture hub blockage effects, the rotor geometry was cut off at $0.20R$ and the remaining components such as the blade attachments and pitch links have been ignored.

Figure 5 shows a top and side view of the computational meshes. The red boundaries denote the no-slip walls of the rotor blades. The green mesh indicates the trimmed unstructured near-body mesh used to model the cylinder hub. This mesh is solved with FUN3D. The cyan mesh is the structured mesh solved by OVERFLOW for the two rotor blades. The black mesh denotes the off-body Cartesian mesh that is solved by SAMCART. The wake is resolved with a single fixed refinement box with a resolution of $dx = dy = dz = 5\%c_{tip} = 0.0021$ m, where c_{tip} is the airfoil chord at the blade tip. This fixed refinement box extends to $z/R = -1.25$. Outside the fixed refinement box, the mesh is progressively coarsened by a factor of 2 in all directions. A 0.25° time step was used for the CFD simulation.

4 Results: overall wake structure and blade tip vortices

In the first part of the discussion, the velocity data from the two vertical PIV measurement planes and the simulation are used to characterize the general wake structure by means of

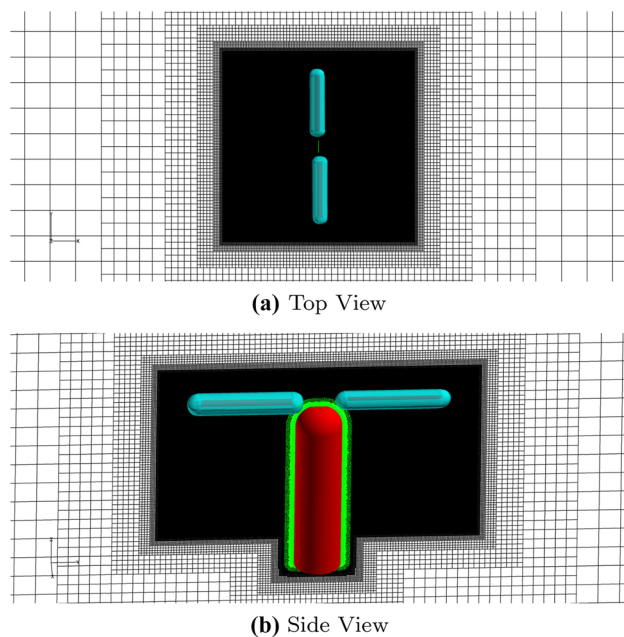


Fig. 5 Top and side views of the computational meshes

averaged and instantaneous data and to assess the agreement of simulation and experiment on key wake parameters.

Averaged velocity fields from 2000 individual PIV recordings for both vertical FOVs are depicted in Fig. 6a. The streamlines represent the in-plane velocity components (v, w), and the contour plot the absolute magnitude of the velocity $V_{xyz} = \sqrt{u^2 + v^2 + w^2}$ (derived from the individually averaged components). The origin of the coordinate system is located in the rotor disk plane ($z/R = 0$) at the position of the rotor hub ($y/R = 0$), as shown in Fig. 4. The velocities are normalized with the hover-induced velocity $V_h = 4.98$ m/s. Figure 6b shows sample phase-averaged velocity fields from a total of 50 individual recordings that were triggered at a wake age of $\psi = 8^\circ$. The blade tip vortices can be detected both by circular streamline patterns and by local velocity peaks. The exact positions of the vortex centers can be identified based on flow field operators that take on extreme values in the vortex core (Bauknecht et al. 2015). Common operators include the vorticity ω_x , the eigenvalues of the velocity gradient tensor λ_2 , the signed swirling strength λ (discriminant of the characteristic equation Q (Zhou et al. 1999) assigned with sense of vortex rotation), and variations thereof (Jeong and Hussain 1995; Adrian et al. 2000; van der Wall and Richard 2006). For the present study, the vortex centers for each individual vortex were detected using the Q -criterion, where Q represents the second invariant of the velocity gradient tensor (Chen et al. (2015), see also next section and Eq. 3). In the phase-averaged velocity fields (Fig. 6b), the mean vortex centers derived from all individually detected center positions for each vortex are marked

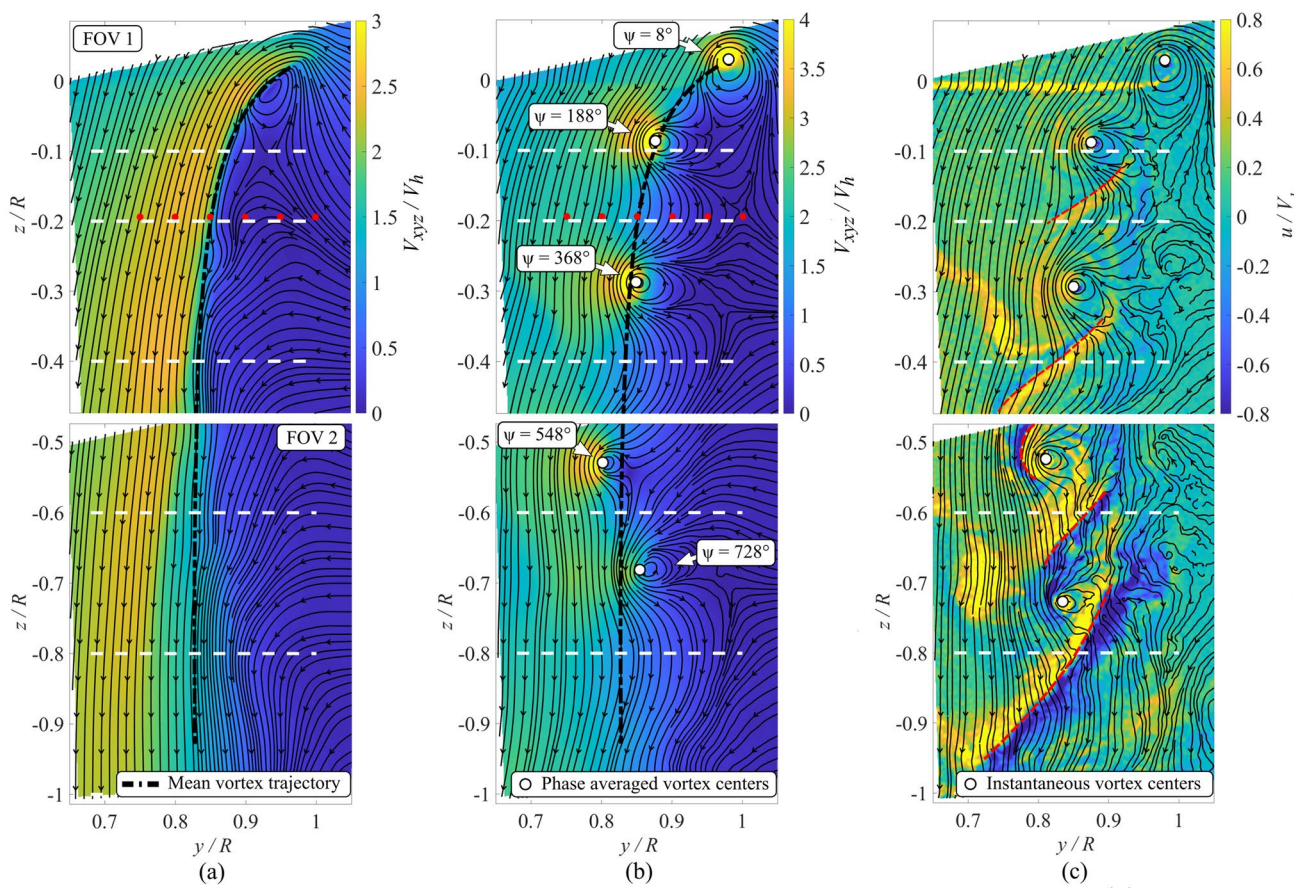


Fig. 6 Measured velocity fields for vertical PIV planes depicting time-averaged velocity fields (a), sample phase-averaged velocity fields from 40 recording cycles (b), and sample instantaneous veloc-

ity fields (c). The horizontal PIV measurement planes are indicated by dashed white lines and the CTA sensor positions corresponding to Fig. 8 by red markers (●)

with white circles. A fitted mean vortex trajectory that is based on all phase-averaged vortex positions is included as a black dashed line. In both fields of view, a total of 5 blade tip vortices with a maximum vortex age of $\psi = 728^\circ$ can be detected. When examining the corresponding velocities, it can be noted that especially for the oldest vortex in Fig. 6b the velocity peak is less distinct. This can be attributed both to the vortex aging process and to an increased variation in the individual vortex positions causing smearing in the phase average. This increased variation is partly a result of a vortex pairing process that becomes more noticeable with increasing wake age. Vortex pairing refers to a pair-wise interaction of consecutive blade tip vortices and has been observed in a number of rotor wake studies (Tangler et al. 1973; Lee et al. 2010; Milluzzo et al. 2010; Schwarz et al. 2019). It results in an altered vortex trajectory and ultimately in a leapfrogging, merging, or breakdown process of a vortex pair. Figure 6c depicts the samples of instantaneous velocity fields at the same wake age of $\psi = 8^\circ$. While the streamlines again represent the components of the in-plane velocity, the

contour plot depicts the out-of-plane velocity u . The blade shear layer is visible as a band of positive velocity which convects downstream. For the youngest blade tip vortex, the shear layer is still connected to the vortex. (See vortex with $\psi = 8^\circ$ in Fig. 6c.) Since the downward convection motion inboard of the slipstream boundary is about twice as fast as for the tip vortices, the blade shear layer at one point catches up to the preceding blade tip vortex.

During this process, the outboard part of the shear layer is stretched between the two tip vortices in an “S”-shaped layout. Indications for this can be observed in the positive out-of-plane velocity band spanning between the second and third tip vortex in Fig. 6c. The blade tip vortex center positions that were detected in the instantaneous velocity fields are again marked with white circles. From the stretched part of the shear layer, the secondary vortex braids are supposed to emerge according to Chaderjian (2012). By tracking the shear layer parts spanning between the blade tip vortices up to higher wake ages, it can be observed that in contrast to the unidirectional and positive out-of-plane velocity of

the blade shear layer, parallel bands of out-of-plane velocity with different sign emerge. These bands indicate the occurrence of vortices with their axis orientation parallel to the measurement plane. The inferred centerlines of the vortices are marked with dashed red lines.

The structure of these wormlike secondary vortices can be better observed in the visualization from the simulation results that were derived in the current study. Figure 7 shows the predicted vorticity magnitude isosurfaces ($|\omega| = 170 \frac{1}{s}$) colored by vertical velocity w . A quarter of the flowfield has been removed to help show the interaction of the vortex sheet with the primary tip vortices. The horizontal PIV measurement planes are shown by green slices. Their location is also included as dashed white lines in Fig. 6. In general, the occurring secondary vortex development in Fig. 7 resembles the vortex structure that was observed, for example, by Wolf et al. (2019b) and Bodling and Potsdam (2020).

To characterize the wake and compare the results from the experiment and the simulation, velocity profiles were extracted. The solid lines in Fig. 8a and c depict the time-averaged velocity profiles at $z/R = -0.194$. The axial position was chosen in order to allow for a direct comparison with velocity data measured for the same rotor settings with constant temperature anemometry (CTA) at radial locations ranging from $y/R = 0.75$ to $y/R = 1.0$. (See marked positions (●) in Fig. 6.) The CTA data provide a significantly higher temporal sampling rate in comparison with the PIV data and thus include the majority of the energy cascade of the turbulent flow. To enable a direct comparison with the recorded CTA data, Fig. 8a depicts the time-averaged profiles of the instantaneous velocity component in the y , z -plane $V_{yz} = \sqrt{v^2 + w^2}$. The general structure and the position of the slipstream boundary show good agreement between the PIV and CTA measurements. The maximum velocity is slightly smaller in the CTA data. The comparison between the PIV results and the simulation, which is

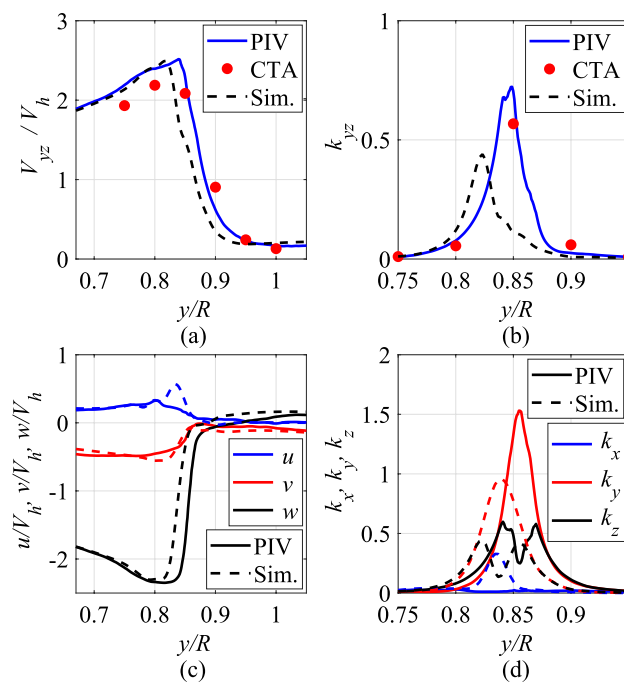
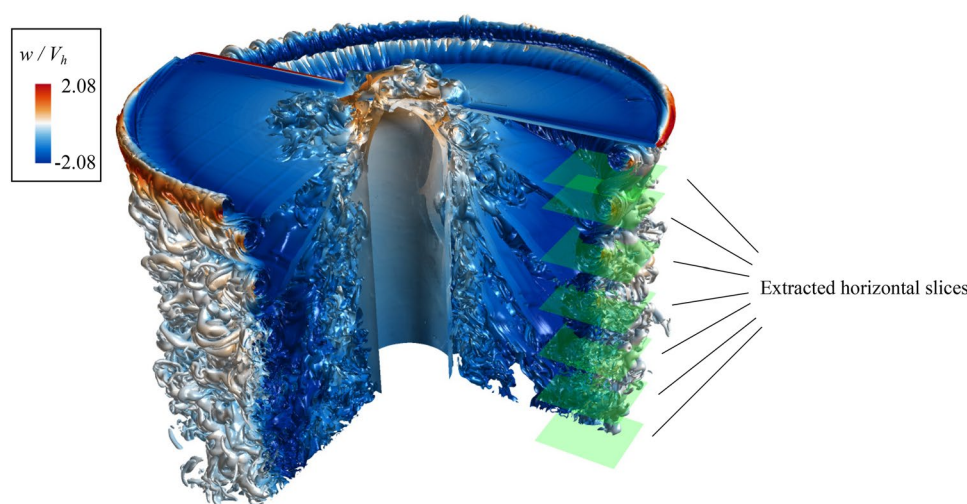


Fig. 8 Comparison of velocity (a+c) and turbulent kinetic energy (TKE) (b+d) profiles along the radial direction at an axial position of $z/R = -0.194$

Fig. 7 Vorticity magnitude isosurfaces ($|\omega| = 170 \frac{1}{s}$) from the simulation, colored by vertical velocity w



included as dashed line, shows a good agreement regarding its shape and absolute values. A slight spatial offset can be observed, which can be the result of low-frequency fluctuations in the wake position. The wake boundary seems to be less smeared out compared to the data from a previous experiment with the same rotor system operated in an enclosure in ground effect reported by Wolf et al. (2019b), which indicates that fewer aperiodic fluctuations are present in the current experiment. This also results in an improved agreement between the experimental and the numerical

data in comparison with the results reported by Bodling and Potsdam (2020). The component-wise decomposition of the velocity profiles in Fig. 8c also is consistent between the simulation and the PIV data, especially regarding the v - and w -components. For the u -component, a deviation at the slipstream boundary location can be observed, which could be the result of particle voids in the vortex cores, where no reliable velocity information could be captured.

The fluctuation level of the velocity can be expressed by the non-dimensionalized turbulent kinetic energy k . For a comparison with CTA data, the turbulent kinetic energy (TKE) in the y, z -plane was derived from the velocity data measured with CTA and PIV as well as from the simulations:

$$k_{yz} = \frac{1}{2V_h^2} \overline{V_{yz}^2}. \quad (1)$$

The turbulent kinetic energy for the individual velocity components is derived analogously by

$$k_x = \frac{1}{2V_h^2} \overline{u'^2}, k_y = \frac{1}{2V_h^2} \overline{v'^2}, k_z = \frac{1}{2V_h^2} \overline{w'^2}. \quad (2)$$

Despite the lower acquisition rate of PIV compared to CTA, the turbulent kinetic energy k_{yz} depicted in Fig. 8b compares relatively well between the two measurement techniques, suggesting that despite the lack of data within the blade tip vortex core the PIV measurements provide reliable data on the turbulent characteristics of the wake. The PIV data can be used to additionally analyze the individual components k_x , k_y and k_z , which are shown in Fig. 8d. When comparing the TKE from the PIV data with the simulation, it can be found that the simulation exhibits lower peak values (39% for k_{yz} , 37% for k_y). A reason for this deficit in TKE could be the smaller maximum swirl velocity of the blade tip vortices that is discussed in the next paragraph (Fig. 9b). As opposed to the preceding study in ground effect (Wolf et al. 2019b), the radial component k_y is significantly higher than the axial component k_z both in the experiment and in the simulation. The most distinct difference between the experimental and the numerical data is the lower k_x value in the PIV results. Analogous to the discrepancy in the absolute u -velocity, this could be the result of particle voids in the vortex cores.

A key wake feature that has to be characterized when analyzing secondary vortex structures and comparing numerical simulations and experiments are the main blade tip vortices. Several researchers have investigated the properties of these vortices, especially since PIV has become the state-of-the-art measurement technique for many aerodynamic applications including helicopter aerodynamics (Raffel et al. 2017). Blade tip vortex parameters were experimentally analyzed, for example, by Ramasamy and Leishman (2006), Ramasamy et al. (2009a), Richard et al. (2006), Mula et al. (2013), Wolf et al. (2019a), and Braukmann et al. (2020).

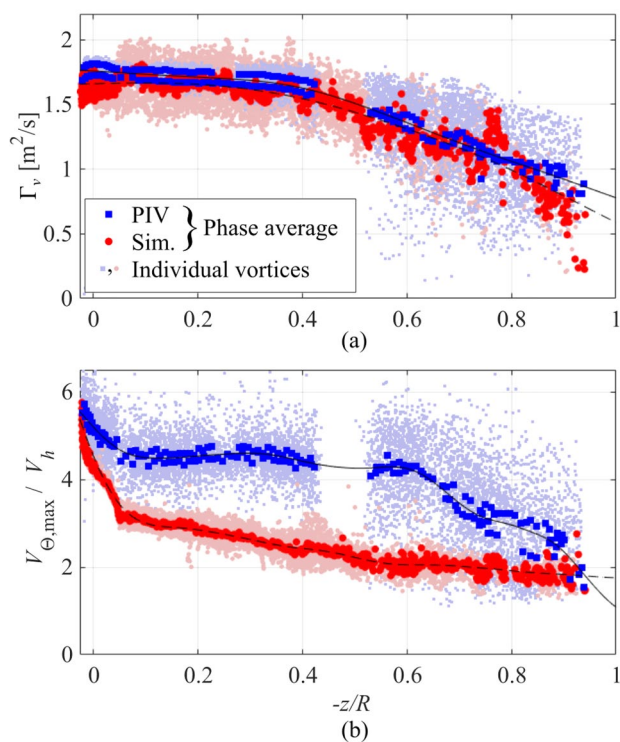


Fig. 9 Blade tip vortex circulation Γ_v (a) and maximum swirl velocity $V_{\theta,\max} / V_h$ (b) over axial position $-z/R$

One characteristic vortex parameter that is typically identified is the swirl velocity V_θ around the vortex core. To extract the swirl velocity, the Cartesian velocity data were transformed in polar coordinates and decomposed into radial and azimuthal components according to Bauknecht et al. (2017). The azimuthal velocities assigned to a vortex radius r were subsequently averaged, and, therefore, a single averaged radial V_θ -profile was calculated for each vortex in the instantaneous flow fields. From these swirl velocity profiles, two main parameters were derived. The first is the circulation Γ_v at large distances from the vortex. In order to avoid the extracted circulation being compromised by neighboring vortices, a radial distance of $0.5 r/c$ from the vortex center was chosen to extract the circulation values. Similar to the methodology applied by Wolf et al. (2019a), Braukmann et al. (2020), and Goerttler et al. (2020), this value is taken as an estimate for the total vortex circulation Γ_v at large radii. The circulation values for all individual blade tip vortex segments that were captured at all analyzed time steps for both the experiment (■) and the simulation (●) are depicted in Fig. 9a over their axial location. For the experimental data, 50 rotor revolutions were analyzed and 10163 individual vortices were extracted with a maximum wake age of 1030° . For the simulation, a total of 6890 individual vortices were extracted stemming from five rotor revolutions that were sampled at a rate of 1° azimuth. Additionally,

phase-averaged values for each wake age were derived and are plotted as blue and red markers (●, ●). Smoothing spline fits were applied to the phase-averaged data and are depicted as solid and dashed black lines. Overall, there is good agreement between the data from the PIV measurements and the simulation. The numerically simulated vortices show slightly lower circulation values compared to the experiment ($\approx 6\%$ lower at the initial stages), which is likely due to the underpredicted thrust coefficient C_T in the simulation ($\approx 10\%$ lower). However, the overall trend is captured well in the simulation. For the experimental data, two sets of data with an offset of 5% can be distinguished in the phase average values. They correspond to the two rotor blades and indicate a slightly different blade loading during rotation. In both the experiment and simulation, the circulation remains relatively constant up to a downstream distance of $z/R = -0.4$ ($\psi = 460^\circ$). For the second FOV, covering downstream distances below $z/R = -0.5$, the circulation values decrease and reach a minimum average value of about 45% of the maximum initial values.

The second blade tip vortex parameter that was extracted is the maximum swirl velocity $V_{\theta,\max}$. The corresponding values for each vortex are depicted in Fig. 9b. Again, the phase-averaged values are included as blue and red markers. Here, a larger discrepancy between experiment and simulation can be observed. Directly after the vortex formation, the maximum swirl velocity in the simulation is higher in comparison with the experiment, with individual vortices exhibiting values up to $12 V_h$ (not visible in Fig. 9b). However, the numerically derived values for $V_{\theta,\max}$ decrease rapidly with increasing vortex age and coincide with the highest experimentally measured values at an axial distance of $0.02 R$ above the rotor plane. Farther downstream, the maximum swirl velocity of the simulated vortices drops below the measured values and is about 33% lower at a distance of $0.1 R$ below the rotor plane. Lim et al. (2012) showed that the grid resolution is an important factor for preserving the strength of the vorticity. In particular, Lim et al. observed that a finer near-body mesh resulted in a less steep drop in maximum vorticity. Considering that at a wake age of 20° , there are roughly seven grid points across the core diameter, the initial divergence in the maximum swirl velocity could be due to not sufficiently resolving the tip vortex in the simulations as it convects through the near-body and off-body mesh. This also affects the size of the vortex core. In the simulation, the core radius grows rapidly within the first 35° wake age to 9.4 mm, which is 80% larger than the measured value for the same wake age. However, despite the differences in the absolute values of $V_{\theta,\max}$, both datasets show a similar trend with a sharp decrease up to an axial distance of $-z/R = 0.07$ corresponding to a wake age of 180° . After this sharp decrease, in the experiment, the swirl velocity settles at a relatively constant value of $V_{\theta,\max} = 4.5 V_h$, while in

the simulation there is a more steady decline. In the experiment, only at a height below $z/R = -0.6$ ($\psi > 600^\circ$), the maximum swirl velocity exhibits a significant drop. A similar observation of the maximum swirl velocity remaining almost constant over a large vortex age range was also made by Schwarz et al. (2019) for an investigation in ground effect and was attributed to vortex stretching due to the nearby ground. Although there is a divergence in the development of the maximum swirl velocity, the good agreement in the vortex circulation up to high vortex ages of $\psi \approx 900^\circ$ at $z/R = -0.93$ suggests that the decay process of the tip vortex system is well captured in the simulations. Based on the good representation of the blade tip vortex system and wake structure in the simulation, the next section will deal with the secondary vortex analysis.

5 Results: secondary vortices

To investigate the development of secondary vortex structures spanning between the blade tip vortices, data from seven horizontally oriented measurement planes were recorded using PIV. The planes were located at axial distances ranging from $z/R = -0.1$ to $z/R = -1.2$ below the rotor, as indicated in Figs. 3, 4, and 6. Instantaneous sample velocity fields are depicted in Fig. 10 at six different axial positions. The vectors represent the components of the in-plane velocity (u, v) showing every sixteenth velocity vector in both x/y -directions, while the contour plot reflects the corresponding vorticity ω_z . The projected track of the blade tip is indicated in Fig. 10a as well as the centerline of the blade tip vortex when passing through the measurement plane. As indicated in the pictogram in Fig. 10a, the velocity fields were recorded roughly 3 ms (24°) before the passage of the center of a blade tip vortex through the measurement plane. The footprints of the blade tip vortices are visible as bands of high velocity in the y -direction. For the lower axial positions at $z/R = -0.8$ and $z/R = -1.0$ (Fig. 10e and f), the blade tip vortex positions are increasingly aperiodic and less coherent, making an exact determination of the blade tip vortex position more difficult. With increasing distance from the rotor plane, the out-of-plane vorticity increases. Areas of increased vorticity can be found starting from a downstream distance of $z/R = -0.2$ mostly on the outboard side of the blade tip vortex. Secondary vortex structures with both signs of rotation emerge and are visible both as vorticity peaks and through the curvature of the in-plane velocity vectors. The number of vortices as well as the vorticity magnitude increases at distances of $z/R = -0.4$ and below. Individual vortices were detected (see next section for the scheme) and are highlighted with green circles for all sample velocity fields in Fig. 10. Their total number is given in the upper right corner of each figure. Similar to the findings of Wolf et al. (2019b) and Bodling and Potsdam

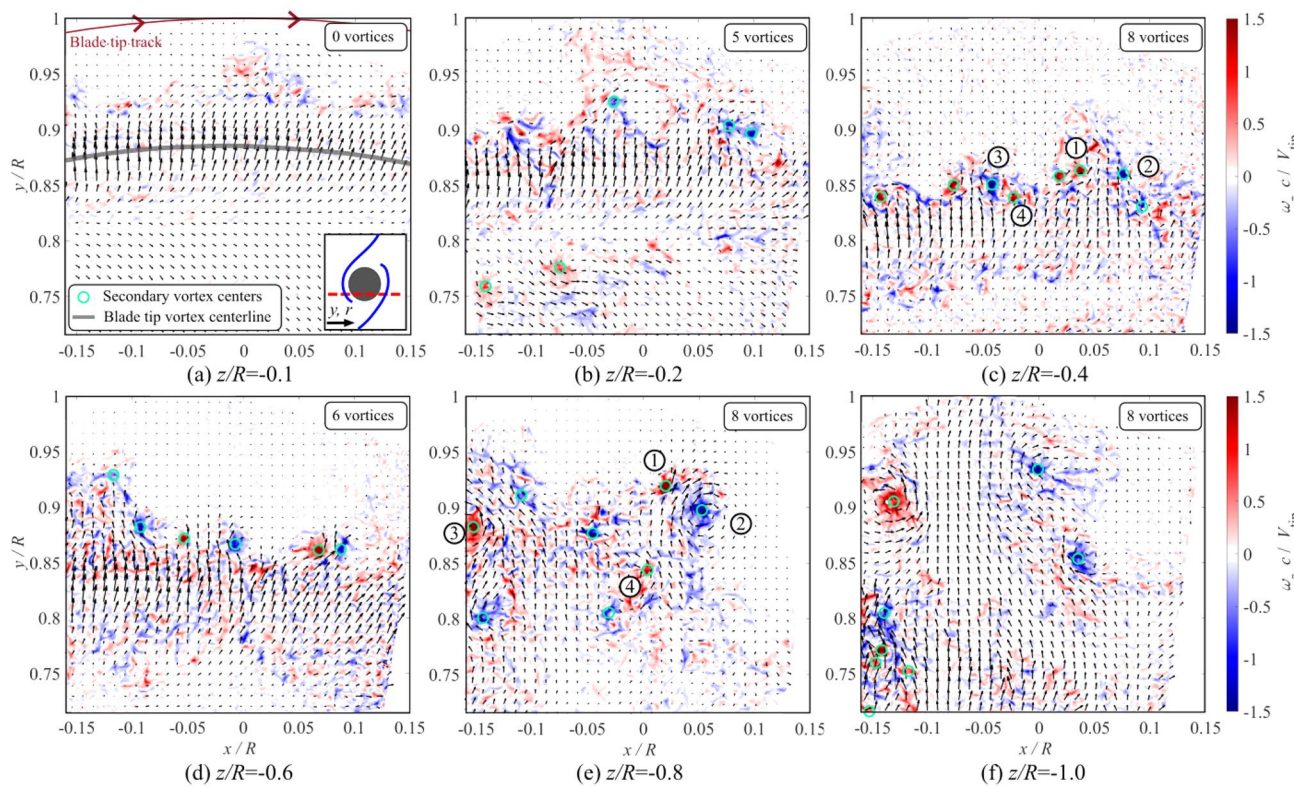


Fig. 10 Instantaneous velocity fields measured with PIV at different axial positions. The vectors represent the in-plane velocities (u , v), and the contour plot the out-of-plane vorticity ω_z . The velocity fields

were recorded about 24° before the passage of a blade tip vortex through the respective measurement plane. For the labeled secondary vortices, see Fig. 13

(2020), pairs of counterrotating vortices are visible, especially in Fig. 10c, d, and f, which result in radially outward directed jets in the in-plane velocity. This is especially evident for the lowest depicted axial location at $z/R = -1.0$ (Fig. 10f). The corresponding flow pattern can be connected to the formation of three-dimensional hairpin braids which evoke the breakdown of the helical blade tip vortex system. The disintegration of the tip vortices into smaller braids or hairpin vortices was, for example, observed by Jain in high-fidelity simulations of the Sikorsky S-76 rotor (Jain 2018). As he points out, a similar phenomenon was also observed in direct numerical simulations of vortex rings (Archer et al. 2008).

5.1 Secondary vortex detection

The current study aims to provide a quantitative analysis of the development and the characteristics of the secondary vortex structures in the rotor wake. Therefore, analogous to the discussion of the blade tip vortex parameters, a vortex identification scheme was applied that identifies the centers of the individual vortices. Similar to the secondary vortex detection scheme used by Wolf et al. (2019b) and Bodling and Potsdam (2020), the Q -criterion was applied to the velocity fields. It was derived based on the assumption of a 2D velocity gradient

tensor from the in-plane velocity components (u , v) according to Chen et al. (2015) by

$$Q = \frac{\partial u}{\partial x} \frac{\partial v}{\partial y} - \frac{\partial u}{\partial y} \frac{\partial v}{\partial x} - \frac{1}{2} \left(\frac{\partial u}{\partial x} + \frac{\partial v}{\partial y} \right)^2. \quad (3)$$

The Q values were calculated based on velocity fields that were postprocessed using a 2D median filter with a size of 4.14 mm in both spatial directions to suppress measurement noise. Only areas exceeding a threshold of $Q = 10^5 \cdot \frac{1}{s^2}$ were accepted, while all lower values were set to zero. Additionally, the “bwpropfilt” function in MATLAB was used to only accept connected areas exceeding the Q -threshold that feature a minimum minor axis length of 4.14 mm. The identical evaluation scheme was used for both the experimental and the numerical data. As shown in Fig. 12, the vortex detection scheme was compared to the 3D Q -criterion isosurfaces from the numerical data to ensure that the detected vortices were physical. The detected vortices in the sample extraction plane (Fig. 12c) indeed correspond to elongated wormlike vortex structures, as can be observed in Fig. 12b, where the cut plane is superimposed with the corresponding zoomed-in region from a Q -isosurface visualization.

Figure 11 depicts the post-processed result for a series of three velocity fields both from the experiment (left column) and the simulation (right column). The flow fields were captured with a time separation of 4.23 ms ($\approx 32^\circ$) for an axial position of $z/R = -0.4$. The physical size of the shown flow field excerpts is the same for both sets of data.

The contour plots represent the signed Q values $Q_s = Q \cdot \frac{\omega_z}{|\omega_z|}$, which includes the sense of rotation of the vortices. The result from Fig. 11e corresponds to the same sample that is depicted in Fig. 10c and illustrates the effect of the filtering and vortex detection scheme. The velocity fields at time step t_1 (Fig. 11a+b) were recorded 56° after the passage of a blade tip vortex center through the measurement plane. The footprint of the blade tip vortex is still visible in the negative v -velocity component that dominates the flow field. The detected secondary vortex centers are marked by white markers. Their radial position groups around the

position of the blade tip vortex passage. The centerlines of the two primary vortices that pass the analyzed plane before (“vortex 1”) and after (“vortex 2”) the depicted measurements were taken are indicated by dashed lines. As the wake convects downward (Fig. 11c+e), the secondary vortex structures are detected farther outboard, which indicates their S-shaped structure shown in Fig. 12.

The depicted numerical data were extracted at the same instants in time as the experimental data with respect to the passage of the first blade tip vortex through the depicted plane. The positions of the detected secondary vortices are similar to the experiment and feature the same outboard shift as the wake convects downward. The areas containing Q values are larger, while the peak values are smaller in comparison with the experiment.

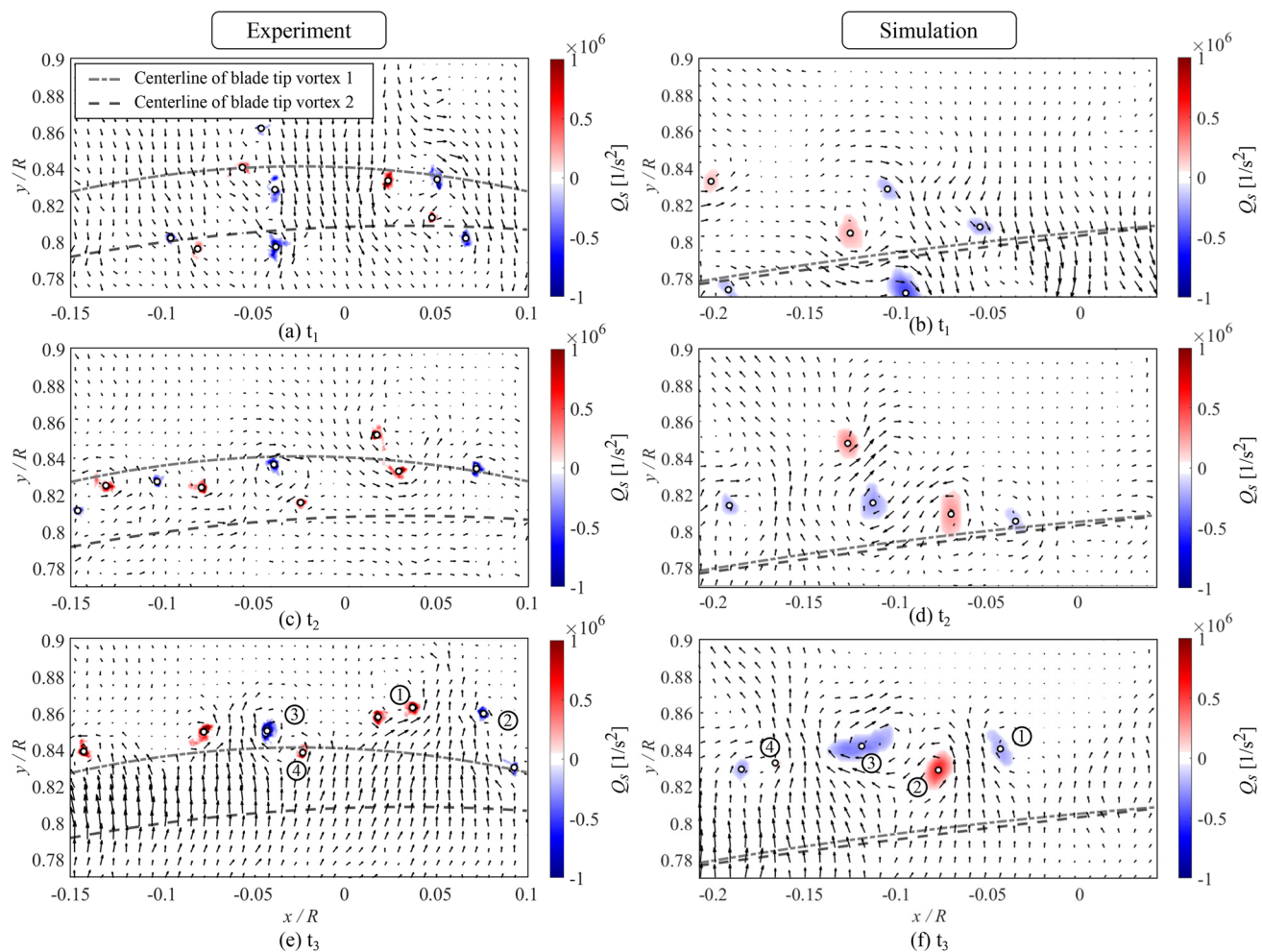


Fig. 11 Sample velocity fields at three consecutive instances in time separated by 32° wake age from experiment (left) and simulation (right) at $z/R = -0.4$. The contours represent the signed Q values

after applying the filtering scheme for secondary vortex detection. Time step t_3 in the experiment (e) corresponds to Fig. 10c; for the labeled vortices, see Fig. 13a-d

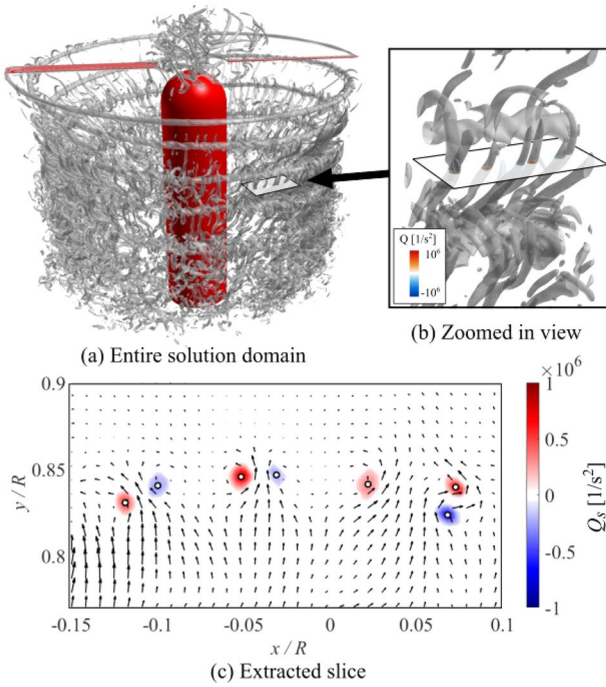


Fig. 12 Visualization of secondary vortex structures and their detection in the extracted slice for the simulation data

5.2 Secondary vortex parameters

Analogous to the blade tip vortex evaluation, vortex parameters were extracted for the secondary worms based on the detected vortex centers and the swirl velocity profiles around these centers. In the same way as for the blade tip vortices, the Cartesian velocity data were decomposed into radial and azimuthal components and subsequently averaged over the azimuthal position. Sample swirl velocity profiles V_θ of secondary vortices that were detected in both the experiment and the simulation are depicted in the left column of Fig. 13; the corresponding circulation values over the radial coordinate are plotted in the right column. For the experimental data, profiles corresponding to the marked vortices in Fig. 10c ($z/R = -0.4$) and Fig. 10e ($z/R = -0.8$) are shown. The depicted profiles from the simulation (Fig. 13c+d) belong to the marked vortices in Fig. 11f at $z/R = -0.4$.

While the swirl velocity profiles in the $z/R = -0.4$ case show peak values in the range of $V_\theta = 0.63 V_h$ to $V_\theta = 0.94 V_h$, the $z/R = -0.8$ case exhibits in part significantly higher maximum swirl velocities up to $V_\theta = 1.24 V_h$. The differences in the experimentally detected swirl velocity profiles in Fig. 13 illustrate the variety of secondary vortices that occur simultaneously at the same wake age. This is also reflected in the vortex core radius (radial position of the maximum swirl velocity), which ranges from $r_c = 0.04 c$ to $r_c = 0.14 c$ for the depicted experimentally measured profiles. The depicted velocity profiles from the simulation in

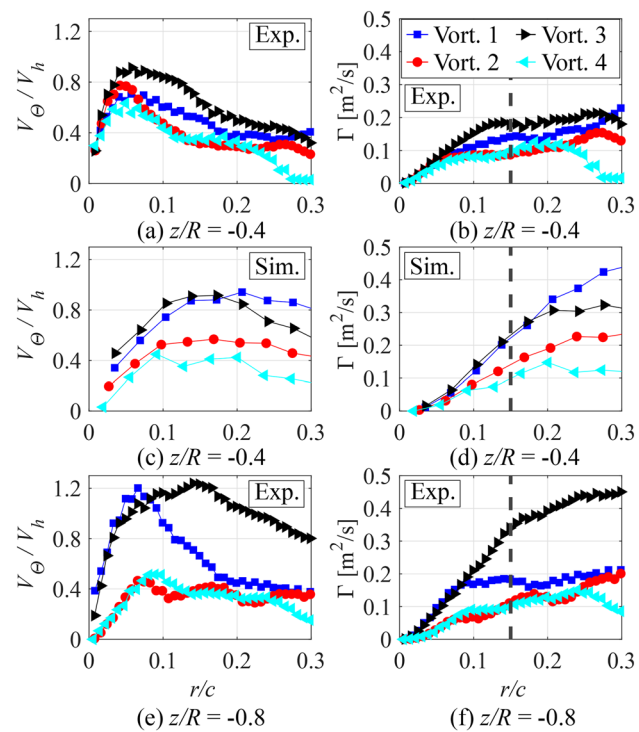


Fig. 13 Sample swirl velocity and circulation profiles of secondary vortex structures from the experiment (a, b, e, f) and the simulation (c, d) corresponding to the $z/R = -0.4$ (a–d) and $z/R = -0.8$ plane (e, f). The corresponding vortices are marked in Fig. 10c,e and Fig. 11e,f

Fig. 13c show in tendency similar maximum swirl velocities as in the experiment at $z/R = -0.4$, but feature larger core radii and thus smaller swirl velocity gradients. This corresponds to the larger “blobs” in the Q -distribution with lower peak values that were found for the simulation (Fig. 11). Due to the lower spatial resolution (i.e., larger grid size) of the numerical data, the velocity profiles also consist of less data points (1/4 as many points).

Analogous to the swirl velocity, the circulation profiles vary depending on the individual vortices. After a steep increase for small radial distances from the vortex center, the circulation Γ reaches a plateau for larger radii. The circulation values that are reached at this plateau correspond to roughly $\Gamma \approx 0.2 \text{ m}^2/\text{s}$ for sample vortices at $z/R = -0.4$ in the experiment (Fig. 13b), while a significantly larger maximum value of $\Gamma \approx 0.45 \text{ m}^2/\text{s}$ is reached for the simulation at the same downstream distance (Fig. 13d) and for vortex 3 in the $z/R = -0.8$ measurement plane. The radial coordinate above which the circulation remains nearly constant again varies for the individual vortices. For the downstream distance of $z/R = -0.4$, the vortex circulation is nearly constant in the experiment above radial distances above $r/c \leq 0.1$, whereas in the simulation and at $z/R = -0.8$ in the experiment the plateau is in part only reached higher

radial distances. For a consistent extraction of the vortex circulation for the entirety of the detected secondary structures, a radial coordinate of $r/c = 0.15$ was chosen in order to capture the most part of the total circulation, but at the same time avoid it being compromised by neighboring secondary structures when choosing larger radial coordinates. (See, for example, vortex 4 in Fig. 13b.) The coordinate is indicated by the dashed lines in Fig. 13.

5.3 Quantitative analysis of secondary vortex structures

To quantitatively investigate the development of the secondary vortex structures, a statistical evaluation was performed for the detected vortex number and the vortex parameters at the measured axial positions from $z/R = -0.1$ to $z/R = -1.2$. For the experimental data, two different sets of measurements were analyzed, which were recorded both in the phase-locked (“series 1”) and in the time-resolved mode (“series 2”). The phase-locked series consists of 4000 samples from 100 recording cycles per axial location, and the time-resolved series comprises 1000 samples for each position. While for the experimental data only segments of the rotor wake covering 16° of the rotor azimuth were measured, the numerical data were evaluated for 360° azimuth. In total, five revolutions were evaluated that were resolved with time steps of 1° resulting in 1800 velocity fields at each axial station. Both the experimental and numerical data were analyzed in a radial band extending from $y/R = 0.68$ to $y/R = 1.01$. The detected vortex number was averaged over all available samples in both experiment and simulation and normalized with the covered azimuth. The average vortex numbers $n_{v,\text{mean}}$ corresponding to an azimuthal range of 360° are shown in Fig. 14 over the axial position in the wake for both the experiment and the simulation. For both datasets, the number of detected vortices increases with increasing downstream distance and reaches its maximum at a distance of $0.8 R$ below the rotor. More distant from the rotor, the number of detected vortices decreases. A possible reason for this can be found in the increasingly less coherent blade tip vortex system and the progressive dissipation of kinetic energy into smaller and smaller-scaled structures. A more detailed discussion on these mechanisms can be found in the next section. (See also Fig. 19.) The total number of detected secondary vortices shows a very good agreement between experiment and simulation up to a downstream position of $z/R = -0.6$. Farther away from the rotor plane, the experimentally detected vortex number exceeds the one from the simulation by 65%–135%. A reason for the higher discrepancy for $z/R \leq -0.8$ could be an increasing effect of vortex pairing that was detected in

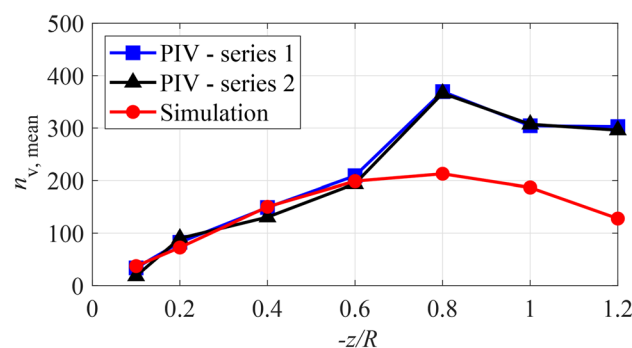


Fig. 14 Average detected vortex number per time step extrapolated to 360° azimuth from experiment and simulation

the experiment and did not occur in the same manner in the simulation.

To gain better insight into the quantitative characteristics and to compare the secondary structures that are detected both in the experiment and in the simulation, the individual vortices were grouped in bins according to both their maximum swirl velocity $V_{\theta,\text{max}}$ and their circulation Γ_v . The resulting histograms are shown in Fig. 15 for both experiment (series 1, ■) and simulation (■) at different downstream positions. For the swirl velocity, only absolute values are considered, whereas for the circulation the sense of rotation is also taken into account in order to analyze a possible preferential direction. The position of the maximum in each of the distributions (●, ●) is detected by applying a Gauss fit (—, —) and extracting the peak in the fitted curve. Both for the maximum swirl velocity and for the circulation, the peak positions are detected at higher values for the simulation compared to the experiment. For the downstream distances from $z/R = -0.1$ to $z/R = -0.6$, the entire distributions seem to be shifted toward larger velocity and circulation values in the simulation. For $z/R = -0.8$ to $z/R = -1.2$, the distributions outward of the detected peak position of the simulated data compare relatively well, but in the experiment significantly more vortices with smaller swirl velocity and circulation are detected, which results in a discrepancy in the overall vortex number at these positions.

The reduced number of weaker vortices in the simulation could be the result of the coarser spatial resolution (1/4 fewer data points). In a previous investigation (Bodling and Potsdam 2020), numerical results that were derived with the same resolution as in the present study were compared to “Shake-The-Box” measurements (Wolf et al. 2019b). In this comparison, the numerically predicted secondary vortex number seemed to be larger than in the experiment, which featured a lower spatial resolution in comparison with the current PIV measurements (Fig. 2). The present experiments indicate that the higher number of worms could be

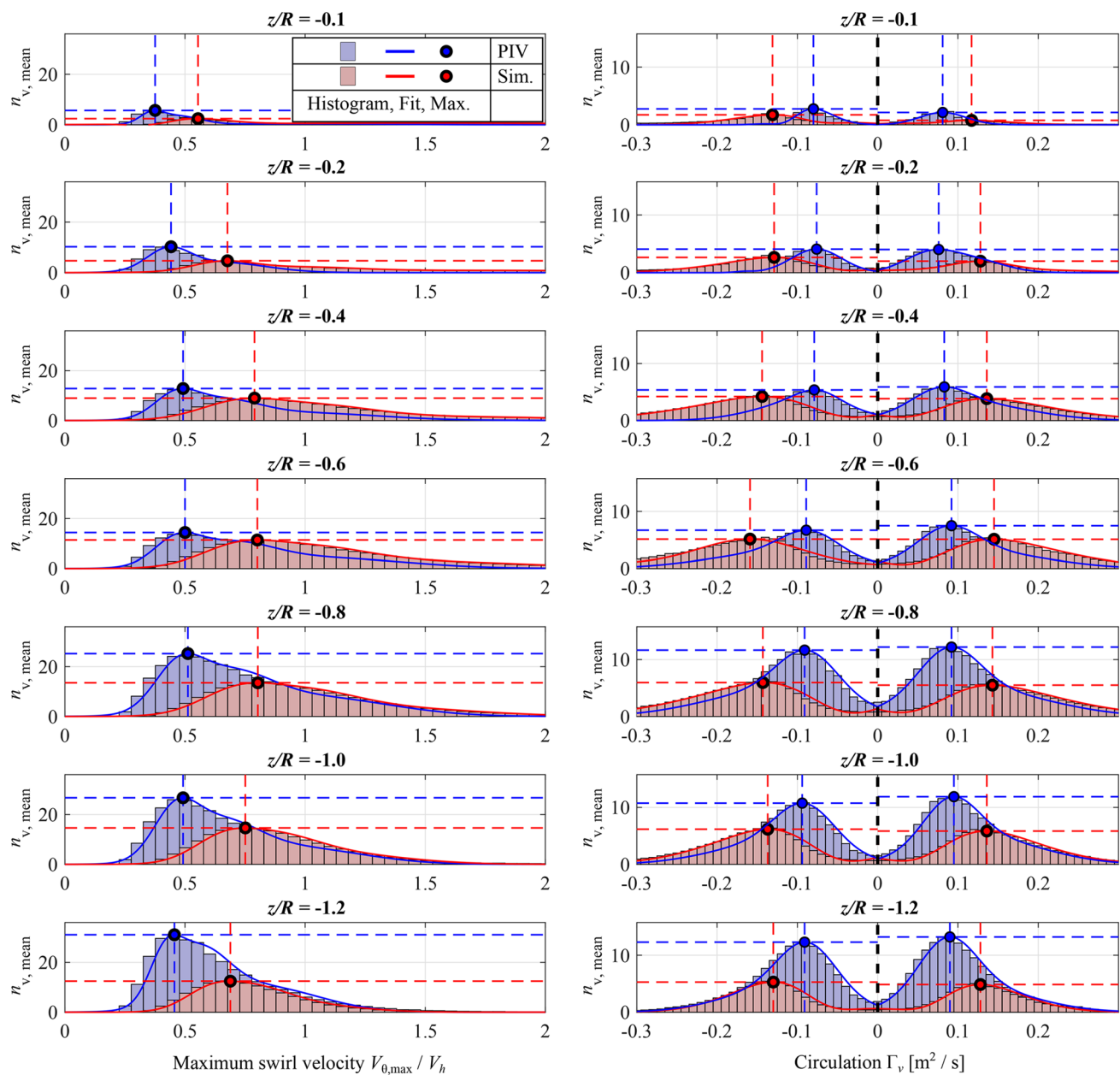


Fig. 15 Secondary vortex histograms corresponding to maximum swirl velocity $V_{\theta,\text{max}}$ (left column) and circulation Γ_v (right column) for different axial positions z/R

physically more accurate. When comparing the positive and negative circulation curves, only a marginal preference in the positive sense of rotation can be detected in the experiment (see horizontal dashed lines), while the numerical data show a similar trend in the opposite direction.

The extracted values of the peak positions for maximum swirl velocity and circulation are plotted in Fig. 16 over the axial position in the wake. Due to the smaller number of weaker vortices that are detected, the peak positions of $V_{\theta,\text{max}}$ and Γ_v are consistently smaller in the experiment than in the simulation. The highest values are reached around

$z/R = -0.6$ to $z/R = -0.8$. The highest number of secondary vortices detected in the PIV data has maximum swirl velocities in the range of $V_\theta = 0.38 V_h - 0.51 V_h$, whereas in the simulation they lie between $V_\theta = 0.55 V_h$ and $V_\theta = 0.8 V_h$.

As for the circulation, the majority of the secondary vortices in the experimental data exhibit values from $\Gamma_v = 0.08 \text{ m/s}^2$ to $\Gamma_v = 0.09 \text{ m/s}^2$, which is roughly 5% of the initial circulation of the blade tip vortices. In the simulation, the peaks are located in a range from $\Gamma_v = 0.12 \text{ m/s}^2$ to $\Gamma_v = 0.16 \text{ m/s}^2$ and thus at about 8% of the blade tip vortex circulation.

In summary, it can be stated that the overall development of secondary structures that was detected in the experiment is quantitatively well represented in the simulation, although weaker structures are not resolved to the same degree as in the experiment. Nonetheless, the results underline the physical validity of secondary vortex structures that appear in high-fidelity CFD simulations.

5.4 Secondary vortex formation and development

Building on the quantitative similarity of experiment and simulation, this section aims to combine the information from both datasets to gain insight into the formation and development process of the secondary vortex structures. One question that is frequently addressed is the development of these structures, which are commonly believed to originate from the blade shear layers.

Chaderjian and Buning argue that the axial stretching of the shear layer between two consecutive tip vortices augments the secondary worm's rotation due to conservation of momentum (Chaderjian and Buning 2011). Therefore, it is suggested that the worms are likely to occur in a phase where a blade shear layer approaches a preceding tip vortex. The measurements by Wolf et al. (Wolf et al. 2019b) demonstrated that first secondary vortices occurred at a wake age of $\psi = 75^\circ$, where the "S"-shaped shear-layer stretching between both tip vortices has not yet developed. Bodling & Potsdam (Bodling and Potsdam 2020) showed that the first secondary vortex structures originate from the shear layer being wrapped around its corresponding primary vortex and breaking apart into coherent structures. This can also be observed in the current simulation data.

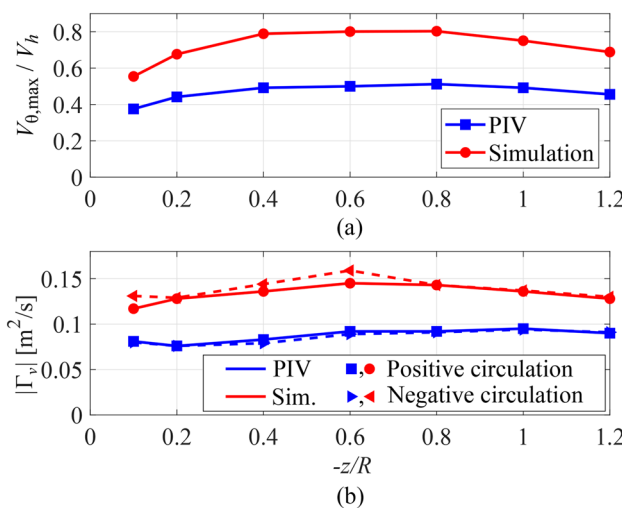


Fig. 16 Peak positions of $V_{\theta,\max}$ (a) and Γ_v (b) from histograms depicted in Fig. 15 over axial position z/R

Figure 17 shows the numerically predicted vorticity magnitude isosurfaces ($|\omega| = 170 \frac{1}{\text{m}}$) at the key stages of the evolution process, $\psi = 5^\circ, 35^\circ, 75^\circ, 115^\circ$, and 150° . Isosurfaces are colored by vertical velocity w/V_h . At $\psi = 5^\circ$, the vortex sheet shed from the blade wraps around the nearby primary vortex. At $\psi = 35^\circ$ and 75° , the vortex sheet breaks apart into small coherent structures while also convecting downward. Small-scale secondary vortices tangling around the blade tip vortex can thus be detected before the shear layer has reached the preceding blade tip vortex. At $\psi = 115^\circ$ and 150° , the shear layer is entrained into the next primary vortex, similar to a classic mixing mechanism in shear layers (Chaderjian and Buning 2011). This causes the shear layer to break apart into the elongated S-shaped coherent structures that are frequently called "worms." Additionally, larger secondary vortex braids can be observed that do not extend between two consecutive blade tip vortices but omit one vortex and connect two primary vortices originating from the same rotor blade. These structures can be observed in the zoomed-in regions in Fig. 17. The underlying mechanism seems to be that as a new blade tip vortex is created and approaches the secondary vortex braids that span between preceding tip vortices (①), parts of the secondary structures get entrained into the newly created blade tip vortex and form the observed elongated structures (②). A similar observation of individual secondary vortices persisting over an extended period $\geq 180^\circ$ azimuth was also made in the PIV data.

The effect of an increased number of secondary vortices in direct proximity to the blade tip vortices is also detected in the current experimental data. Figure 18 depicts the phase-dependent evolution of the average number of secondary vortices $n_{v,\text{mean}}$ for the four upper measurement planes from $z/R = -0.1$ to $z/R = -0.6$. The phase-locked PIV data were used to calculate an average number from 100 samples that were recorded for each phase position. The phase position is expressed using the azimuthal progression relative to azimuth at which the first blade tip vortex passes through the respective measurement plane ("relative wake age"). The phase positions at which the blade tip vortex centers were located in the measurement planes were detected based on the radial (v) velocity components and are marked by black dashed lines in Fig. 18a-d. The number of detected secondary vortices shows peaks in close proximity to the tip vortex passages for all depicted axial planes. The secondary vortex number is up to six times higher around the blade tip vortices than at phase positions between two tip vortices (Fig. 18b). One of the reasons for that can be found in the fact that worm structures on both sides of the blade tip vortex are detected that span to the preceding and subsequent blade tip vortex. (See, for example, Fig. 12b.) Also, at the position where the measurement plane cuts through the

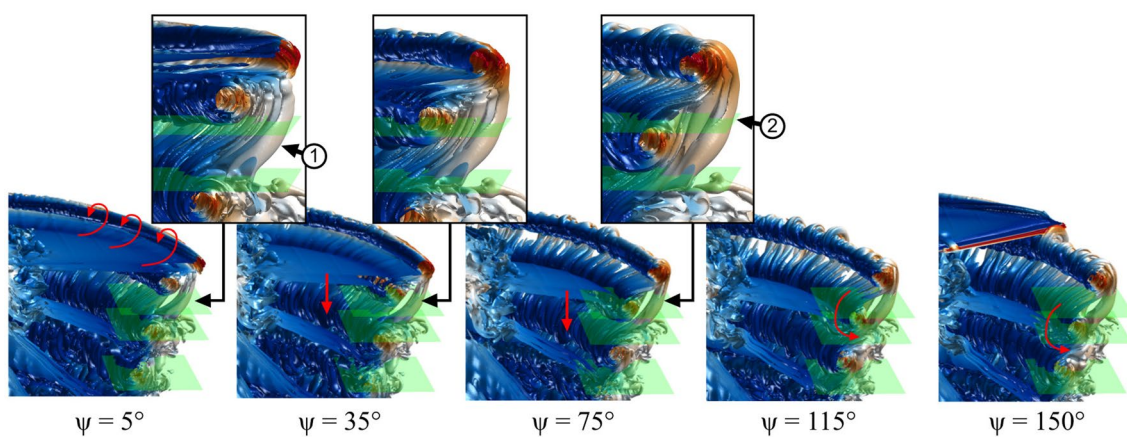


Fig. 17 Secondary vortex development process ranging from rotor wake age $\psi = 5^\circ$ to $\psi = 150^\circ$, visualized with data from the simulation

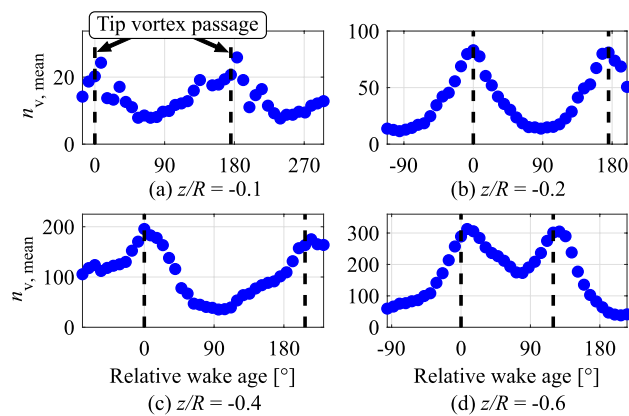


Fig. 18 Experimentally detected average vortex number over phase position denoted with wake age relative to the passage of the first blade tip vortex

center of a tip vortex, the secondary structures are oriented perpendicular to the measurement plane, whereas at different phase positions the vortices are cut in a more oblique way due to their S-shaped structure. Nonetheless, the surplus of detected secondary structures around the primary vortex supports the finding of an increased number of secondary structures tangling around the primary vortices.

A second aspect that is investigated here is the development of the secondary structures with increasing wake age and its connection to the stability of the blade tip vortex system. In Fig. 14, it was shown that both in the experiment and in the simulation the number of secondary vortices is maximum at an axial coordinate of $z/R = -0.8$ and decreases for higher downstream distances. To better understand this process, Fig. 19 shows how the secondary vortices evolve as they convect downstream.

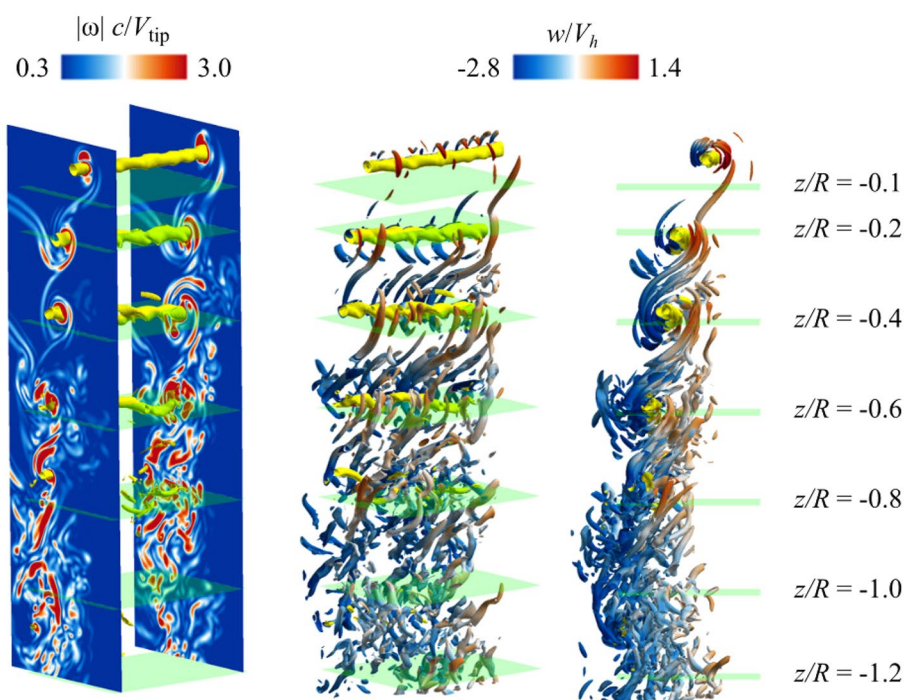
As shown in the left side of Fig. 19, the primary vortices break down in the simulation for $z/R \leq -0.6$, as indicated

by the increasingly disorganized tip vortices. The corresponding variation of the secondary vortices along the axial direction is shown in the middle and right side of the figure. The primary vortex is shown in the yellow Q-criterion iso-surfaces with $Q = 10^6 \cdot \frac{1}{s^2}$, and the clockwise rotating secondary vortices are colored by vertical velocity w/V_h with $Q = 10^5 \cdot \frac{1}{s^2}$ (counter-clockwise vortices omitted for clarity). As discussed before, the measured data show that for small wake ages ($z/R \geq -0.6$), the secondary vortices are concentrated around the primary tip vortex. However, we see that as shown in the right side of Fig. 19, when the primary vortex starts to break down, the S-shape of the secondary vortices starts to become more chaotic. While the secondary worms still appear in an organized pattern above $z/R = -0.6$, the breakdown of the tip vortices below $z/R = -0.8$ seems to facilitate the dissipation of the worms into smaller and more chaotic structures, which will tend to break down with increasing age. As the primary vortex breaks down, the secondary vortices become less concentrated around the primary vortex and this leads to fewer secondary vortices. As previously discussed, pairing effects were detected in the PIV data (Fig. 6). Therefore, differences in how the primary vortex breaks down in the simulation and experimental data could explain why there is a higher discrepancy in the total number of secondary vortices for $z/R \leq -0.8$.

6 Conclusions

A joint experimental and numerical investigation was performed to analyze and quantify the development of secondary vortex structures in the wake of a two-bladed rotor out of ground effect. High-speed PIV experiments were conducted to capture velocity fields with both vertical and horizontal measurement planes to capture a large portion of the wake and to resolve the blade tip vortices as well as secondary

Fig. 19 Simulation-based visualization of tip vortex breakdown (left) and variation of secondary vortices along the axial direction (middle and right). For clarity, only the clockwise rotating secondary vortices are shown



vortex structures. Simultaneously, a high-fidelity simulation with Helios was conducted. First, the overall wake structure in terms of the downwash velocities and the blade tip vortex system was analyzed and compared between experiment and simulation. In a second step, a combined experimental and numerical investigation of secondary vortex structures wrapping around and spanning between the blade tip vortices was performed. The following conclusions have been drawn from this collaborative experimental and computational study:

1. Average downwash velocity profiles showed a good agreement between the experimentally captured PIV data and the simulation regarding both the magnitude and the spatial distribution of the velocity. There was satisfactory agreement in the turbulent kinetic energy, where the radial velocity component showed the largest differences.
2. The blade tip vortices were characterized for downstream distances up to 0.93 rotor radii below the rotor plane. Although an initial divergence in the maximum swirl velocity was observed, the good agreement in the vortex circulation up to high vortex ages of $\psi \approx 900^\circ$ at $z/R = -0.93$ suggests that the decay process of the tip vortex system was well captured in the simulations.
3. Secondary vortex structures were experimentally detected in seven horizontal measurement planes that were distributed over a downstream distance of $1.2 R$ below the rotor. Corresponding planes were analogously analyzed in the CFD data. The application of identical evaluation schemes for both the experiment and the
4. Simulation allowed for a direct quantitative comparison. The overall vortex number that was detected showed good agreement, indicating that the conducted Helios simulations are capable of correctly modeling the phenomenon despite the underprediction of $V_{\Theta,\max}$. It was found both in the experiment and in the simulation that the number of vortices increased to a downstream distance of $z/R = -0.8$ where it showed a peak value. At larger downstream distances, where the blade tip vortex system is found to become increasingly chaotic, the number of detected secondary structures decreases.
5. Secondary vortex parameters were extracted, and a statistical evaluation showed that for the more intense secondary vortex structures, good agreement between simulation and experiment was achieved. In the PIV data, however, a larger number of less intense secondary structures were detected which could be a result of the higher spatial resolution compared to the simulation. Nonetheless, the results indicate that for the given grid resolution and solver sub-iteration convergence, the secondary vortex phenomenon as a whole is captured well with the high-fidelity simulations. Their influence on the decay of the blade tip vortex system does not seem to be overestimated, as was supposedly the case in a number of recent high-fidelity simulations. Future studies on grid convergence and grid resolution will be needed to confirm what is sufficient to capture the secondary vortex phenomenon.
6. Investigation of the development process of the secondary vortices showed an intensified formation of second-

ary structures around the blade tip vortices, where the simulation data showed their emergence from the rolled-up blade shear layer. This was supported by a statistical evaluation of the experimental data that showed an increased number of secondary vortices in the measurement plane in direct proximity to the blade tip vortices. This is also detectable at higher vortex ages up to the point where vortex pairing hampers the identification of individual primary vortices. No distinct preferential direction of rotation was detected neither in the experimental data nor in the CFD simulation. The instantaneous velocity fields instead regularly showed pairs of vortices with alternating sense of rotation.

For the first time, since high-fidelity CFD simulations identified previously unseen secondary vortex structures in helicopter wakes, there is now both qualitative and quantitative experimental corroboration with computation of their existence, strength, and number. This study contributed to a more fundamental understanding of their development, behavior, stability, and decay.

The results have opened up many areas for further research. Variations in thrust and blade number change the tip vortex separation distance in the helical wake. Therefore, in future work we will investigate how the development of the secondary vortices is affected by thrust and blade number variations. Other topics for future research include the role of turbulence and wake sheet strength in the secondary vortex development process. Additionally, it can be addressed how the secondary vortices exactly affect primary tip vortex breakdown and how their occurrence is related to instability mechanisms such as long-wave and short-wave instabilities.

Acknowledgements The experimental part of the study was conducted in the framework of the DLR project “URBAN-Rescue.” The authors thank M. Krebs, J. Braukmann, A. Kostek, and F. Lößle, for their help in preparing and executing the rotor tests. The simulations presented in this paper are a product of the CREATE™-AV Element of the Computational Research and Engineering for Acquisition Tools and Environments (CREATE) Program sponsored by the US Department of Defense HPC Modernization Program Office. Computational resources provided by the DoD High Performance Computing Modernization Office, Army S/AAA Roger Strawn, are greatly appreciated. The common research benefited from decades of cooperation in the framework of US-German MoUs between US Army, NASA, and DLR.

Funding Open Access funding enabled and organized by Projekt DEAL.

Open Access This article is licensed under a Creative Commons Attribution 4.0 International License, which permits use, sharing, adaptation, distribution and reproduction in any medium or format, as long as you give appropriate credit to the original author(s) and the source, provide a link to the Creative Commons licence, and indicate if changes were made. The images or other third party material in this article are included in the article's Creative Commons licence, unless indicated otherwise in a credit line to the material. If material is not included in

the article's Creative Commons licence and your intended use is not permitted by statutory regulation or exceeds the permitted use, you will need to obtain permission directly from the copyright holder. To view a copy of this licence, visit <http://creativecommons.org/licenses/by/4.0/>.

References

- Abras J, Hariharan NS (2021) Direct volume visualization for deeper insights on the physics of 3d vorticity dynamics in the wake of a hovering rotor. In: AIAA science and technology forum and exposition, Virtual, AIAA 2021-0734, <https://doi.org/10.2514/6.2021-0734>
- Abras J, Hariharan NS, Narducci RP (2019) Wake breakdown of high-fidelity simulations of a rotor in hover. AIAA science and technology forum and exposition. San Diego, CA, USA
- Adrian RJ, Christensen KT, Liu ZC (2000) Analysis and interpretation of instantaneous turbulent velocity fields. *Exper Fluids* 29(3):275–290. <https://doi.org/10.1007/s003489900087>
- Archer PJ, Thomas TG, Coleman GN (2008) Direct numerical simulation of vortex ring evolution from the laminar to the early turbulent regime. *J Fluid Mech* 598:201–226. <https://doi.org/10.1017/S0022112007009883>
- Bauknecht A, Ewers B, Schneider O, Raffel M (2015) Aerodynamic results from the star hover test: an examination of active twist actuation. In: 41st European Rotorcraft Forum, Munich, Germany
- Bauknecht A, Ewers B, Schneider O, Raffel M (2017) Blade tip vortex measurements on actively twisted rotor blades. *Exper Fluids* 58(49). <https://doi.org/10.1007/s00348-017-2312-3>
- Bernal L, Roshko A (1986) Streamwise vortex structure in plane mixing layers. *J Fluid Mech* 170:499–525. <https://doi.org/10.1017/S002211208600099X>
- Biedron RT, Carlson J, Derlaga JM, Gnoffo PA, Hammond DP, Jones WT, Kleb B, Lee-Rausch EM, Nielsen E, Park M, Rumsey C, Thomas J, Thompson KB, Wood W (2019) Fun3d manual: 13.6. NASA TM 220416
- Bodling A, Potsdam M (2020) Numerical investigation of secondary vortex structures in a rotor wake. In: Vertical flight society 75th annual forum, virtual
- Braukmann JN, Wolf CC, Goerttler A, Raffel M (2020) Blade tip vortex system of a rotor with cyclic pitch. *AIAA J* 58(7):2869–2880. <https://doi.org/10.2514/1.J058678>
- Buning P, Nichols R (2021) User’s manual for overflow 2.3. <https://overflow.larc.nasa.gov/users-manual-for-overflow-2-3/>
- Chaderjian NM (2012) Advances in rotor performance and turbulent wake simulation using des and adaptive mesh refinement. In: Seventh international conference on computational fluid dynamics (ICCFD7), Big Island, HI, USA
- Chaderjian NM, Buning P (2011) High resolution navier-stokes simulation of rotor wakes. American helicopter society 67th annual forum. Virginia Beach, VA, USA
- Chen Q, Zhong Q, Qi M, Wang X (2015) Comparison of vortex identification criteria for planar velocity fields in wall turbulence. *Phys Fluids* 27(085101). <https://doi.org/10.1063/1.4927647>
- Comte P, Silvestrini J, Bégou P (1998) Streamwise vortices in large-eddy simulations of mixing layers. *Eur J Mech B/Fluids* 17(4):615–637. [https://doi.org/10.1016/S0997-7546\(98\)80016-2](https://doi.org/10.1016/S0997-7546(98)80016-2)
- Egolf A, Hariharan NS, Narducci RP, Reed E (2017) Aiaa standardized hover simulation: Hover performance prediction status and outstanding issues. In: 55th AIAA aerospace sciences meeting, grapevine, TX, USA, American institute of aeronautics and astronautics, AIAA 2017-1429, <https://doi.org/10.2514/6.2017-1429>

- Goerttler A, Braukmann JN, Wolf CC, Gardner AD, Raffel M (2020) Blade tip-vortices of a four-bladed rotor with axial inflow. *J Am Helicopter Soc* 65(4):1–13. <https://doi.org/10.4050/JAHS.65.042002>
- Gray RB (1992) Vortex modeling for rotor aerodynamics - the 1991 alexander a. nikolsky lecture. *J Am Helicopter Soc* 37(1):3–14. <https://doi.org/10.4050/JAHS.37.1.3>
- Hariharan N, Abras J, Narducci R (2020) An overview of wake breakdown in high-fidelity simulations of rotor-in-hover. In: Vertical flight society 75th annual forum, virtual
- Hariharan NS, Egolf TA, Sankar LN (2014) Simulation of rotor in hover: Current state and challenges. In: 52nd aerospace sciences meeting, national harbor, MD, USA, AIAA 2014-0041, <https://doi.org/10.2514/6.2014-0041>
- Heineck JT, Yamauchi GK, Wadcock AJ, Lourenco L, Abrego AI (2000) Application of three-component piv to a hovering rotortake. In: American helicopter society 56th annual forum. Alexandria, VA, USA
- Jain R (2018) Sensitivity study of high-fidelity hover predictions on the sikorsky s-76 rotor. *J Aircraft* 55(1):78–88. <https://doi.org/10.2514/1.C034076>
- Jeong J, Hussain F (1995) On the identification of a vortex. *J Fluid Mech* 285:69–94. <https://doi.org/10.1017/S0022112095000462>
- Lee B, Baeder JD (2021) The effect of time marching on the wake structure breakdown in a hovering rotor simulation. In: AIAA science and technology forum and exposition, virtual, AIAA 2021-0736, <https://doi.org/10.2514/6.2021-0736>
- Lee TE, Leishman JG, Ramasamy M (2010) Fluid dynamics of interacting blade tip vortices with a ground plane. *J Am Helicopter Soc* 55(22005). <https://doi.org/10.4050/JAHS.55.022005>
- Lim J, Wissink A, Jayaraman B, Dimanlig A (2012) Helios adaptive mesh refinement for hart ii rotor wake simulations. In: American helicopter society 68th annual forum. Fort Worth, TX, USA
- Milluzzo JI, Sydney A, Rauleder J, Leishman JG (2010) In-ground-effect aerodynamics of rotors with different blade tips. In: American helicopter society 66th annual forum, Phoenix, AZ, USA
- Mobley F, Carnes J, Coder JG (2021) Modal decomposition analysis of hovering rotor wake breakdown. In: AIAA science and technology forum and exposition, virtual, AIAA 2021-0737, <https://doi.org/10.2514/6.2021-0737>
- Mula SM, Stephenson JH, Tinney CE, Sirohi J (2013) Dynamical characteristics of the tip vortex from a four-bladed rotor in hover. *Exper Fluids* 54(1600). <https://doi.org/10.1007/s00348-013-1600-9>
- Öhrle C, Schäferlein U, Keßler M, Krämer E (2018) Higher-order simulations of a compound helicopter using adaptive mesh refinement. In: American helicopter society 74th annual forum, Phoenix, AZ, USA
- Potsdam M, Jayaraman B (2014) Uh-60a rotor tip vortex prediction and comparison to full-scale wind tunnel measurements. In: American helicopter society 70th annual forum. Montreal, Canada
- Pulliam TH (1984) Euler and thin-layer navier-stokes codes arc2d and arc3d. Computational fluid dynamics users workshop. University of Tennessee Space Institute, Tullahoma, TN, USA
- Raffel M, Bauknecht A, Ramasamy M, Yamauchi GK, Heineck JT, Jenkins LN (2017) Contributions of particle image velocimetry to helicopter aerodynamics. *AIAA J* 55(9):2859–2874. <https://doi.org/10.2514/1.J055571>
- Ramasamy M, Leishman JG (2006) A generalized model for transitional blade tip vortices. *J Am Helicopter Soc* 51(1):92–103. <https://doi.org/10.4050/JAHS.51.012004>
- Ramasamy M, Johnson B, Huismann T, Leishman JG (2009a) Digital particle image velocimetry measurements of tip vortex characteristics using an improved aperiodicity correction. *J Am Helicopter Soc* 54(012004). <https://doi.org/10.4050/JAHS.54.012004>
- Ramasamy M, Johnson B, Leishman JG (2009b) Turbulent tip vortex measurements using dual-plane stereoscopic particle image velocimetry. *AIAA J* 47(8):1826–1840. <https://doi.org/10.2514/1.39202>
- Richard H, Bosbach J, Henning A, Raffel M, van der Wall B (2006) 2c and 3c piv measurements on a rotor in hover condition. In: 13th international symposium on applications of laser techniques to fluid mechanics, Lisbon, Portugal
- Schanz D, Gesemann S, Schröder A (2016) Shake-the-box: Lagrangian particle tracking at high particle image densities. *Exper Fluids* 57(70). <https://doi.org/10.1007/s00348-016-2157-1>
- Schwarz C, Bauknecht A, Mailänder S, Raffel M (2019) Wake characterization of a free-flying model helicopter in ground effect. *J Am Helicopter Soc* 64(012010). <https://doi.org/10.4050/JAHS.64.012010>
- Shur M, Stelets M, Travin A, Spalart P (2000) Turbulence modeling in rotating and curved channels: Assessing the spalart-shur correction. *AIAA J* 38(5):784–792. <https://doi.org/10.2514/2.1058>
- Sitaraman J, Floros M, Wissink A, Potsdam M (2010) Parallel domain connectivity algorithm for unsteady flow computations using overlapping and adaptive grids. *J Comput Phys* 229(12):4703–4723. <https://doi.org/10.1016/j.jcp.2010.03.008>
- Tangler JL, Wohlfeld RM, Miley SJ (1973) An experimental investigation of vortex stability, tip shapes, compressibility, and noise for hovering model rotors. In: NASA CR-2305
- van der Wall BG, Richard H (2006) Analysis methodology for 3c-piv data of rotary wing vortices. *Exper Fluids* 40(5):798–812. <https://doi.org/10.1007/s00348-006-0117-x>
- Wissink A, Kamkar S, Pulliam T, Sitaraman J, Sankaran V (2010) Cartesian adaptive mesh refinement for rotorcraft wake resolution. In: 28th AIAA applied aerodynamics conference, Chicago, IL, USA, p 4554
- Wissink AM, Dylan J, Jayaraman B, Roget B, Lakshminaray VK, Sitaraman J, Bauer AC, Forsythe J, Trigg RD (2021) New capabilities in create-a-helios version 11. In: AIAA science and technology forum and exposition, virtual, <https://doi.org/10.2514/6.2021-0235>
- Wolf CC, Braukmann JN, Stauber W, Schwermer T, Raffel M (2019a) The tip vortex system of a four-bladed rotor in dynamic stall conditions. *J Am Helicopter Soc* 64(022005). <https://doi.org/10.4050/JAHS.64.022005>
- Wolf CC, Schwarz C, Kaufmann K, Gardner AD, Michaelis D, Bosbach J, Schanz D, Schröder A (2019b) Experimental study of secondary vortex structures in a rotor wake. *Exper Fluids* 60(175). <https://doi.org/10.1007/s00348-019-2807-1>
- Zhou J, Adrian RJ, Balachandar S, Kendall TM (1999) Mechanisms for generating coherent packets of hairpin vortices in channel flow. *J Fluid Mech* 387:353–396. <https://doi.org/10.1017/S002211209900467X>

Publisher's Note Springer Nature remains neutral with regard to jurisdictional claims in published maps and institutional affiliations.

Terms and Conditions

Springer Nature journal content, brought to you courtesy of Springer Nature Customer Service Center GmbH (“Springer Nature”). Springer Nature supports a reasonable amount of sharing of research papers by authors, subscribers and authorised users (“Users”), for small-scale personal, non-commercial use provided that all copyright, trade and service marks and other proprietary notices are maintained. By accessing, sharing, receiving or otherwise using the Springer Nature journal content you agree to these terms of use (“Terms”). For these purposes, Springer Nature considers academic use (by researchers and students) to be non-commercial.

These Terms are supplementary and will apply in addition to any applicable website terms and conditions, a relevant site licence or a personal subscription. These Terms will prevail over any conflict or ambiguity with regards to the relevant terms, a site licence or a personal subscription (to the extent of the conflict or ambiguity only). For Creative Commons-licensed articles, the terms of the Creative Commons license used will apply.

We collect and use personal data to provide access to the Springer Nature journal content. We may also use these personal data internally within ResearchGate and Springer Nature and as agreed share it, in an anonymised way, for purposes of tracking, analysis and reporting. We will not otherwise disclose your personal data outside the ResearchGate or the Springer Nature group of companies unless we have your permission as detailed in the Privacy Policy.

While Users may use the Springer Nature journal content for small scale, personal non-commercial use, it is important to note that Users may not:

1. use such content for the purpose of providing other users with access on a regular or large scale basis or as a means to circumvent access control;
2. use such content where to do so would be considered a criminal or statutory offence in any jurisdiction, or gives rise to civil liability, or is otherwise unlawful;
3. falsely or misleadingly imply or suggest endorsement, approval , sponsorship, or association unless explicitly agreed to by Springer Nature in writing;
4. use bots or other automated methods to access the content or redirect messages
5. override any security feature or exclusionary protocol; or
6. share the content in order to create substitute for Springer Nature products or services or a systematic database of Springer Nature journal content.

In line with the restriction against commercial use, Springer Nature does not permit the creation of a product or service that creates revenue, royalties, rent or income from our content or its inclusion as part of a paid for service or for other commercial gain. Springer Nature journal content cannot be used for inter-library loans and librarians may not upload Springer Nature journal content on a large scale into their, or any other, institutional repository.

These terms of use are reviewed regularly and may be amended at any time. Springer Nature is not obligated to publish any information or content on this website and may remove it or features or functionality at our sole discretion, at any time with or without notice. Springer Nature may revoke this licence to you at any time and remove access to any copies of the Springer Nature journal content which have been saved.

To the fullest extent permitted by law, Springer Nature makes no warranties, representations or guarantees to Users, either express or implied with respect to the Springer nature journal content and all parties disclaim and waive any implied warranties or warranties imposed by law, including merchantability or fitness for any particular purpose.

Please note that these rights do not automatically extend to content, data or other material published by Springer Nature that may be licensed from third parties.

If you would like to use or distribute our Springer Nature journal content to a wider audience or on a regular basis or in any other manner not expressly permitted by these Terms, please contact Springer Nature at

onlineservice@springernature.com